Article

Current Biology

Ultrastructural differences impact cilia shape and external exposure across cell classes in the visual cortex

Graphical abstract

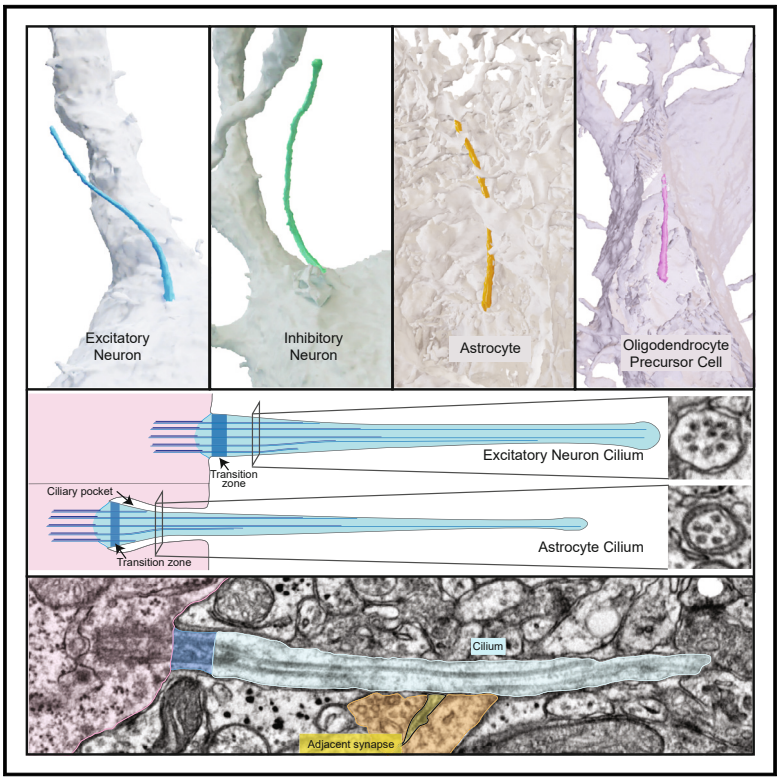

Highlights

- Primary cilia extend from visual cortex neurons and select glia
- Internal cilia ultrastructure is not stereotyped but varies between cell classes
- Cilia are near synapses and surrounded by neurites and glial processes
- Cilia placement and structure impact the external environment of cilia

Authors

Carolyn M. Ott, Russel Torres, Tung-Sheng Kuan, ..., Wei Chung Lee, Nuno Maçarico da Costa, Jennifer Lippincott-Schwartz

Correspondence

ottc@janelia.hhmi.org (C.M.O.), lippincottschwartzj@janelia.hhmi.org (J.L.-S.)

In brief

Ott and Torres et al. identify distinguishing anatomical features of neuronal and glial primary cilia in the mouse visual cortex. Internal structural differences determine both cilium shape and the extent of cilium exposure to the extracellular neuropil, where cilia pass near, and even adjacent to, many synapses.

Ott et al., 2024, Current Biology *34*, 2418–2433
June 3, 2024
https://doi.org/10.1016/j.cub.2024.04.043

CellPress

CellPress
OPEN ACCESS

Current Biology

Article

Ultrastructural differences impact cilia shape and external exposure across cell classes in the visual cortex

Carolyn M. Ott,[1,9,12,*] Russel Torres,[2,9] Tung-Sheng Kuan,[3] Aaron Kuan,[4,8] JoAnn Buchanan,[2] Leila Elabbady,[2,5] Sharmishtaa Seshamani,[6] Agnes L. Bodor,[2] Forrest Collman,[2] Davi D. Bock,[7] Wei Chung Lee,[4] Nuno Maçarico da Costa,[2,10] and Jennifer Lippincott-Schwartz[1,11,*]

[1]Janelia Research Campus, Howard Hughes Medical Institute, Ashburn, VA 20147, USA
[2]Allen Institute for Brain Science, Seattle, WA 98109, USA
[3]Department of Physics, University at Albany, State University of New York, Albany, NY 12222, USA
[4]Department of Neurobiology, Harvard Medical School, Boston, MA 02115, USA
[5]University of Washington, Seattle, WA 98195, USA
[6]Allen Institute for Neural Dynamics, Seattle, WA 98109, USA
[7]Larner College of Medicine, University of Vermont, Burlington, VT 05405, USA
[8]Present address: Department of Neuroscience, Yale School of Medicine, New Haven, CT 06510, USA
[9]These authors contributed equally
[10]X (formerly Twitter): @AllenInstitute
[11]X (formerly Twitter): @JLS_Lab
[12]Lead contact
*Correspondence: ottc@janelia.hhmi.org (C.M.O.), lippincottschwartzj@janelia.hhmi.org (J.L.-S.)
https://doi.org/10.1016/j.cub.2024.04.043

SUMMARY

A primary cilium is a membrane-bound extension from the cell surface that contains receptors for perceiving and transmitting signals that modulate cell state and activity. Primary cilia in the brain are less accessible than cilia on cultured cells or epithelial tissues because in the brain they protrude into a deep, dense network of glial and neuronal processes. Here, we investigated cilia frequency, internal structure, shape, and position in large, high-resolution transmission electron microscopy volumes of mouse primary visual cortex. Cilia extended from the cell bodies of nearly all excitatory and inhibitory neurons, astrocytes, and oligodendrocyte precursor cells (OPCs) but were absent from oligodendrocytes and microglia. Ultrastructural comparisons revealed that the base of the cilium and the microtubule organization differed between neurons and glia. Investigating cilia-proximal features revealed that many cilia were directly adjacent to synapses, suggesting that cilia are poised to encounter locally released signaling molecules. Our analysis indicated that synapse proximity is likely due to random encounters in the neuropil, with no evidence that cilia modulate synapse activity as would be expected in tetrapartite synapses. The observed cell class differences in proximity to synapses were largely due to differences in external cilia length. Many key structural features that differed between neuronal and glial cilia influenced both cilium placement and shape and, thus, exposure to processes and synapses outside the cilium. Together, the ultrastructure both within and around neuronal and glial cilia suggest differences in cilia formation and function across cell types in the brain.

INTRODUCTION

Primary cilia are membrane-enveloped extensions of microtubules that grow from the mother centriole in diverse mammalian cells. Until recently we knew little about structural features of cilia in the brain and how the unique extracellular environment impacts cilia exposure to potential ligands. Early observers hypothesized a sensory role for neuronal cilia,[1,2] which are now known to influence brain function, development, behavior, mood, and cognition.[3–9] Several syndromes caused by defects in primary cilia formation and function include symptoms of impaired physical and cognitive development,[10] and emerging research suggests links between primary cilia and mental health and age-related decline.[11,12]

Primary cilia share common features across all cell types. The ciliary membrane, continuous with the cellular plasma membrane, sheaths the microtubules of the ciliary axoneme, which is anchored to the mother centriole (also called a basal body when a cilium is present). The specialized composition of both the ciliary membrane and cytoplasm is maintained by the transition zone (TZ), a boundary formed by repeating "Y"-shaped protein complexes that ring the microtubules at the base of the cilium.[13] Cilia microtubule doublets extend directly from mother centriole microtubules. Primary cilia are non-motile and lack structures that

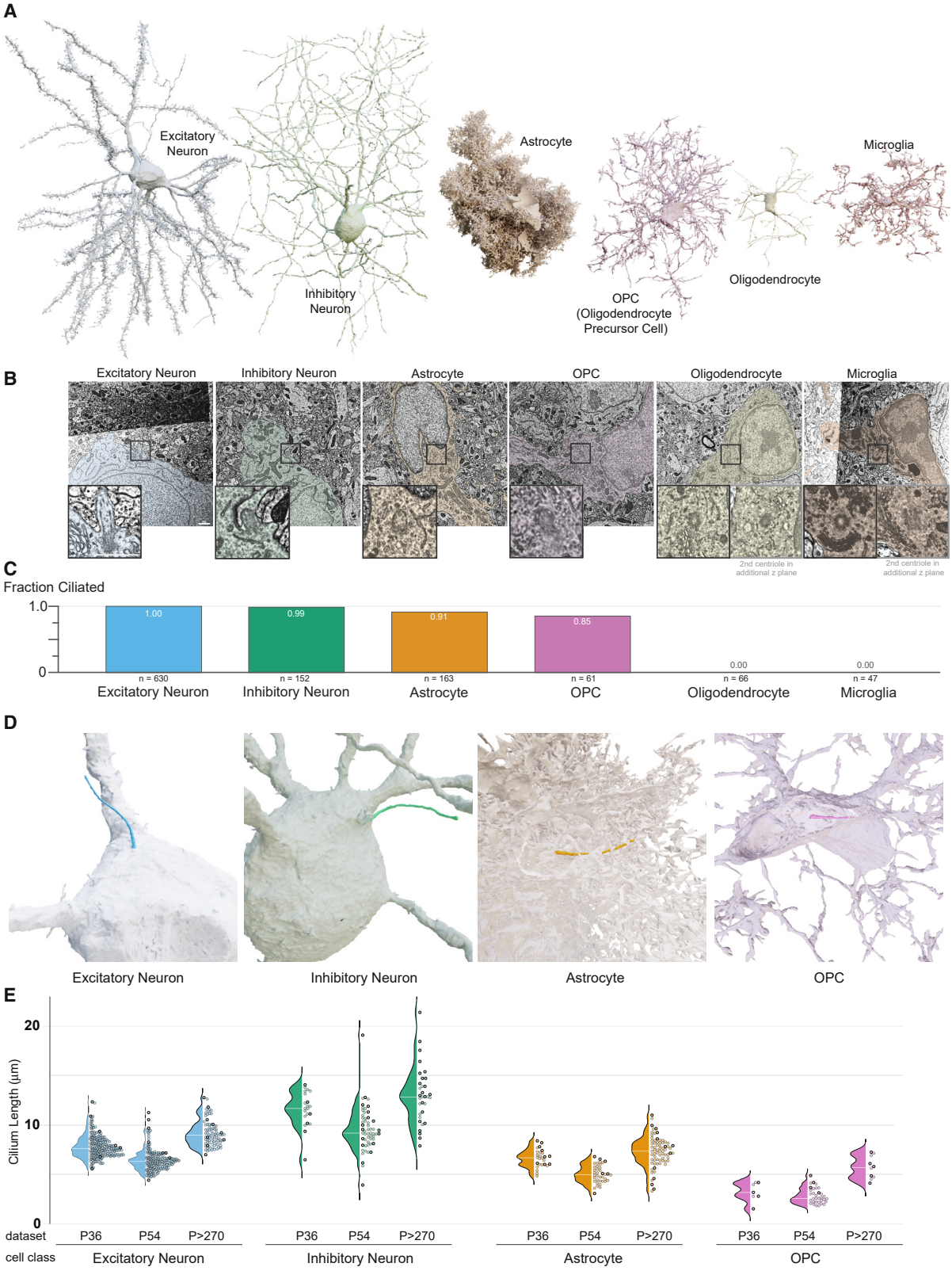

Figure 1. Neurons, astrocytes, and OPCs have primary cilia

(A) Cell class exemplars annotated in this study.

(B) Electron micrographs of basal bodies/centrosomes from cells in (A). Scale bars, 1 μm.

(legend continued on next page)

promote beating in motile cilia. Despite the stereotyped structure of cilia, both classic and emerging data support cell-specific differences in cilia structures in diverse systems and tissues.[14,15] For example, although typically illustrated as extending the entire length of the cilium, microtubule doublets can change and even terminate within a cilium.[16,17] In the visual cortex, the different types of neurons and glia have been grouped into broad cell classes: excitatory or inhibitory neurons, astrocytes, microglia, oligodendrocytes, and oligodendrocyte precursor cells (OPCs). Given the strong links between primary cilia and brain health, we asked whether cilia exhibit structural differences relevant to their function in each of these different cell classes.

Early electron microscopists captured serial sections of a few astrocyte and neuronal cilia.[1,18–20] However, cell-type-specific structural knowledge in the context of neural tissue has been elusive because primary cilia are difficult to locate using conventional electron microscopy (EM) approaches. There is typically only a single cilium per cell, making it unlikely that any given EM thin section through a cell will intersect a cilium. Further, upon exiting the cell, the cilium is hard to distinguish from the surrounding network of glial and neuronal processes, called the neuropil. The neuropil is the context for non-synaptic signal transmission to neuronal and glial cilia, and the neuropil also constrains the cilium. Recently published large-scale-volume EM datasets present an opportunity to view cellular structures in the diverse cell types of the brain. These have already begun to be mined for structural information about cilia.[21–24] In addition, modern computational innovations used to generate three-dimensional (3D) volumes of each cell body and process have provided unprecedented access to multiple quantifiable cellular properties.[21–24] Here, we mine three transmission EM (TEM) volumes of the mouse primary visual cortex (V1)[25–30] to determine primary cilia ultrastructure in hundreds of cells across different brain cell classes. We discovered key anatomical differences between cilia on neurons and glia, including differences in microtubule organization and basal body docking. In addition, we re-imaged selected cilia at higher resolution to resolve differences between excitatory neuron and astrocyte TZs. We characterized the dense extracellular micro-environment surrounding primary cilia and found that cilia pass directly adjacent to synapses. Synapses are not enriched near cilia—rather, cilia stochastically encounter synapses densely populating the surrounding neuropil. We further analyzed physical parameters of cilia, such as shape and orientation, and demonstrated cell-class differences in cilia structure and formation. Together, the new data reveal variations in primary cilia anatomy in the brain, which suggest that cell-type specialization of cilia structures may influence brain development, behavior, mood, and cognition.

RESULTS

Locating cilia in neurons and glia in the visual cortex

We annotated cilia and centrosomes in three EM volumes of mouse visual cortex where cilia are present in their native context.[25,28–32] We refer to the datasets by the age of the mouse: P36, P54, and P>270. While all three datasets targeted V1, they are not replicates (the details of each volume are described in Table S1). Figure 1A shows cellular reconstructions of representative cells from six morphologically defined cell classes. The most prevalent cells were excitatory pyramidal neurons. Several types of inhibitory neurons were observed, including chandelier cells, basket cells, neurogliaform cells, bipolar cells, and Martinotti cells. Glial cells that were observed included astrocytes (both fibrous and protoplasmic), microglia, and cells in the oligodendrocyte lineage, including precursor cells (OPCs) and premyelinating and mature oligodendrocytes. Figure 1B shows EM images of the base of the cilium for the neurons and glia displayed in Figure 1A. Both centrioles are included for the oligodendrocyte and microglia, neither of which were ciliated, which is consistent with other brain regions.[33–35] The extent of ciliation for each cell class is shown in Figure 1C and detailed in Table S2. Magnified 3D reconstructions of cilia are shown in Figure 1D; Video S1.

Cilium length determines how far a cilium extends, its surface area, and its volume. To compare cilia length, we generated and measured skeleton lines along the central path. Path lengths are plotted by cell class for each dataset (Figure 1E). Inhibitory neuronal cilia were the longest and OPC cilia were the shortest. Within each dataset, the average astrocytic cilium length was less than the average excitatory neuronal cilium length. Cilia in P>270 were longer than in P36 or P54 (see Figures 1E and S1A), possibly reflecting individual differences or differences in sample and data preparation that produced minor discrepancies affecting scaling. The layers sampled also contributed to differences between the datasets. For example, the average length of inhibitory neuronal cilia in P36 was comparable to layer 2/3 of P54 (11.6 ± 0.7 μm and 11.6 ± 1.8 μm (95% confidence interval [CI]), but longer than the average length of all P54 inhibitory neurons (9.6 ± 0.6 μm; 95% CI).

We also compared cilia lengths between cell types within classes. P>270 includes 20 fibrous astrocytes—many of which are in layer 1. The cilia of fibrous astrocytes were shorter on average than the cilia of protoplasmic astrocytes (Figure S1A). Inhibitory neurons include many different cell types, some of which were identified in P36 and P54. Cilia lengths from basket cells, bipolar cells, chandelier cells, Martinotti cells, and neurogliaform cells suggest that cilia in individual cell types cluster more strongly than the cell class as a whole (Figure S1B). Inhibitory neurons populate different cortical layers,[36] so both the observed differences in cilia length and the distributions of cilia lengths (plotted by depth in Figure S1C) indicated differences within the inhibitory cell class. Excitatory neuronal cilia also differed in cilia length across layers 2/3–6 (Figure S1C). In layer 5 cilia length variance was larger than in other cortical layers. Together, the measurements revealed cilia length variance between and within cell classes.

(C) Fraction of ciliated cells by class.
(D) Cilia on cells in (A). Astrocyte and OPC were cut away to reveal the cilium.
(E) Cilium length graphed as a distribution (left) and individual values (right).
See also Figure S1 and Video S1.

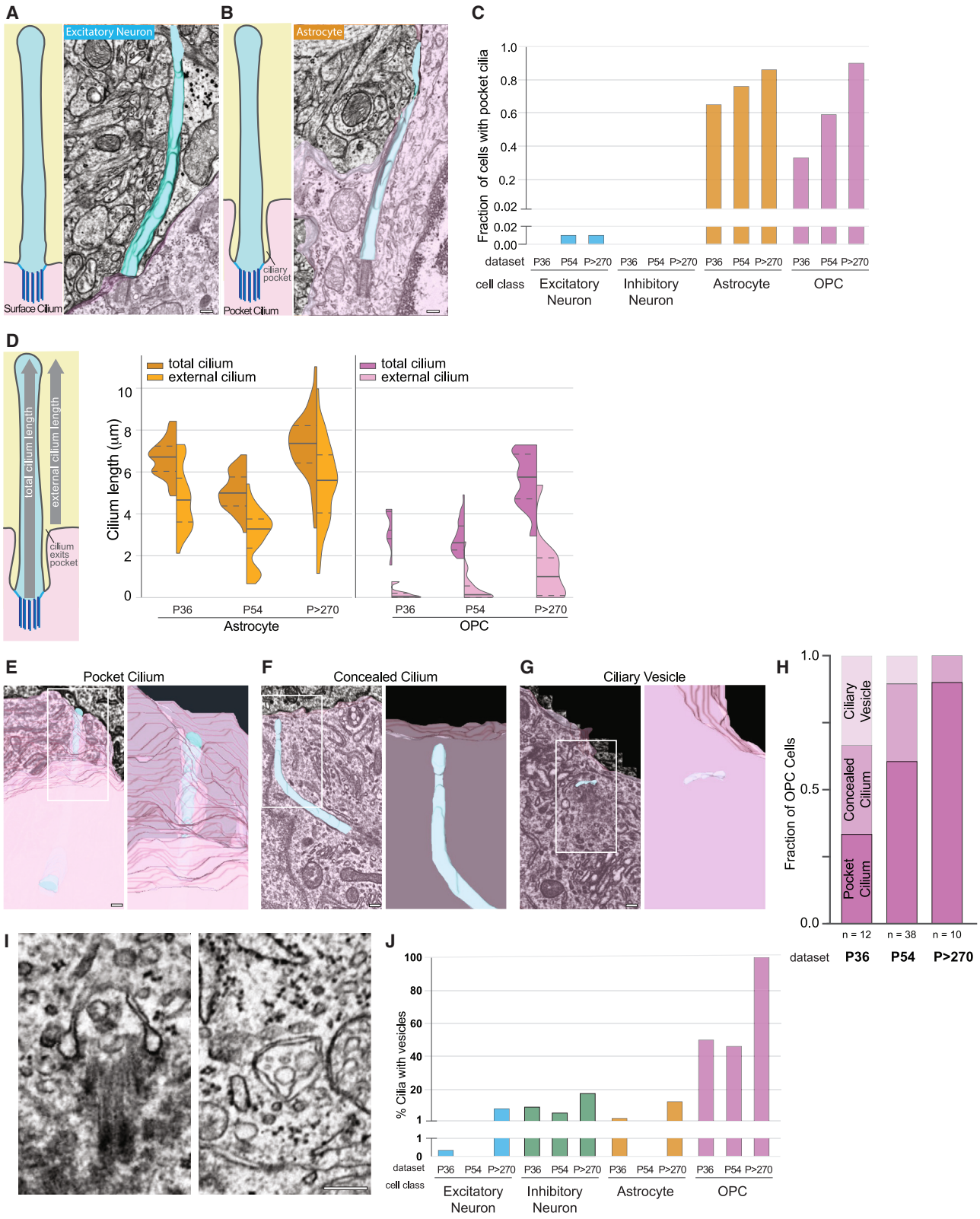

Figure 2. Neurons have surface cilia and most glial cilia have a ciliary pocket

(A and B) Surface and pocket cilia illustrations and segmented representations of an excitatory neuron (A) and an astrocyte (B) cilium. Scale bars, 200 nm.
(C) The fraction of cells with ciliary pockets.

(legend continued on next page)

Ciliary pockets are found predominantly in astrocyte and OPC cells

To understand physical properties of cilia in the cortex, we assessed structural features at the cilium origin. Specifically, some cilia emerged from a centriole docked at the plasma membrane (surface cilium, Figure 2A) while others extended from a centriole recessed in a membrane invagination (pocket cilium, Figure 2B).[1] The cilium biogenesis pathway determines the base structure[37,38] and whether the entire length begins externally exposed or originates as a membrane-enclosed internal structure that retains the encapsulating membrane to form the ciliary pocket.[39] We quantified base structures. With rare exceptions, all neurons had surface cilia (Figure 2C). In contrast, glia predominantly had pocket cilia. We compared the path lengths of the external portion of pocket cilia to the total path lengths (Figure 2D). Generally, astrocyte pockets were ~2 μm. OPC cilia pockets were deeper and the majority of OPC cilia project less than 3 μm from the cell. These data suggest that glial cilia have less exposed signal detecting surface.

Most astrocytes without pocket cilia have surface cilia. However, OPCs without pocket cilia had structures that indicated they were in the process of ciliogenesis or cilia disassembly. To compare these intermediate structures across datasets, we quantified concealed cilia (internal cilia)[40] and ciliary vesicles (vesicles associated with distal appendages) (Figures 2F–2H). We observed a trend that correlated with the age of the mice. Internal structures were unique to OPCs, except a single astrocyte daughter centriole with a ciliary vesicle in P>270.

Vesicles were also found inside cilia (Figures 2I, 2J, and S2). Although infrequent, there are published TEM images of internal vesicles.[21,41–45] Vesicles were rare in astrocyte and neuronal cilia (Figure S2A). In contrast, OPC cilia contained prevalent and diverse vesicles: single-membrane vesicles, double-membrane vesicles, compressed vesicles, round vesicles with transparent contents, and vesicles with dark centers (Figure S2B). All vesicles were adjacent to the ciliary membrane, thus they could not move along the center of the axoneme as proposed.[46] Together, the analysis of cilia nanostructure revealed distinctions between cell classes.

Neuronal cilia had longer TZs than astrocytic cilia

We examined the TZ, the boundary structure at the base of the cilium.[13] When sectioned lengthwise, TZs appear as densities between the membrane and microtubules (Figures 3A and 3B). In cross-sections, the Y-shaped structures of the TZ are referred to as Y-links[47] (Figures 3C and S3). Internal structures were especially clear in the P>270 dataset and our initial impression was that astrocytic TZs were shorter than in neurons, but many TZs were not fully resolved or were sectioned at oblique angles. We used two strategies to try to investigate TZ differences. First, we selected seven cilia in the P>270 dataset found to be primarily aligned—either parallel or perpendicular to the imaging plane—and reimaged these cilia on the original TEM grids at higher resolution, ranging from 0.36 to 0.56 nm/pixel (versus 4 nm/pixel in the original dataset; Figure 3A). TZs of an excitatory neuron and astrocyte are visible in alternating sections due to the periodic nature of the structure. TZ density is longer in the neuron than in the astrocyte (Figure 3B). Fewer consecutive astrocyte cross-sections had visible Y-links than seen in neuronal cilia (Figures 3C, S3A, and S3B). We noted that fibrous astrocytes had electron-dense material, possibly abundant intermediate filaments, filling the center (Figure S3C). The internal staining cleared beyond the TZ.

The second strategy we used was to identify a subset of cilia sectioned approximately parallel to the imaging plane in the P>270 dataset and measure TZ density in every z plane (Figure 3D). Variations in TZ measurements within a single cilium were expected because cutting angles were not perfectly parallel. The weighted mean TZ length for excitatory and inhibitory neurons (286 and 314 nm, respectively) was longer than for astrocytes (168 nm). The process of TZ formation has not yet been examined in brain, but the observed structural differences might be assembly-related as in other tissues.[48–50]

Microtubules and microtubule-binding proteins change along the cilium

It is known that the number and organization of microtubules can change within a cilium.[16,51,52] We noticed that changes in ciliary microtubules differed between excitatory neurons and astrocytes. First, A-tubules had an electron-dense center near the cilium base (diagrammed in Figure 4A) resembling microtubule inner binding proteins (MIPs), recently characterized inside *Chlamydomonas* flagella.[53,54] Beyond the proximal region, the center of the A-tubule appeared translucent, suggesting that the density was restricted to the base of the cilium. The doublets lost the internal A-tubule staining approximately 2.3 μm (excitatory neuron) and 1.2 μm (astrocyte) from the base (Figures 4B and 4C; Video S2). In neurons, the dark to light tubule transition happened once, but in astrocytes, several A-tubules alternated between stained and empty near the base. The changes in microtubule staining can also be seen in cilia cut lengthwise, where doublet staining at the base was darker (Figure S4A).

We tracked microtubule rearrangements within cilia, including shifting of the deviant filament[1] from the periphery into the center of the axoneme (Video S2; Figures S4B and S4C). Termination of B-tubules left singlet microtubules (yellow arrows in right panels of Figure 4B), some of which subsequently terminated. In astrocytic cilia, both doublets and singlets terminated. We captured a side view of doublet termination while re-imaging the TZ at high resolution (Figure S4C). Electron densities on either side of the

(D) Distribution of path lengths, external and in total.
(E–G) Segmented OPC cilium (E), concealed cilium (F), or ciliary vesicle (G). Enlarged regions of interest (ROIs) illustrate that the cilium barely emerges (E) or is completely concealed (F). Scale bars, 200 nm; ROI width: 1,085 nm.
(H) OPC classifications are plotted by dataset.
(I) Vesicles inside OPC cilia. Scale bar, 200 nm.
(J) The percentage of cilia with internal cilia vesicles was graphed for each cell class in each dataset. In (A) and (B) and (E)–(G), cilium, cyan; cell interior, pink; overlaid onto a single EM plane.
See also Figure S2.

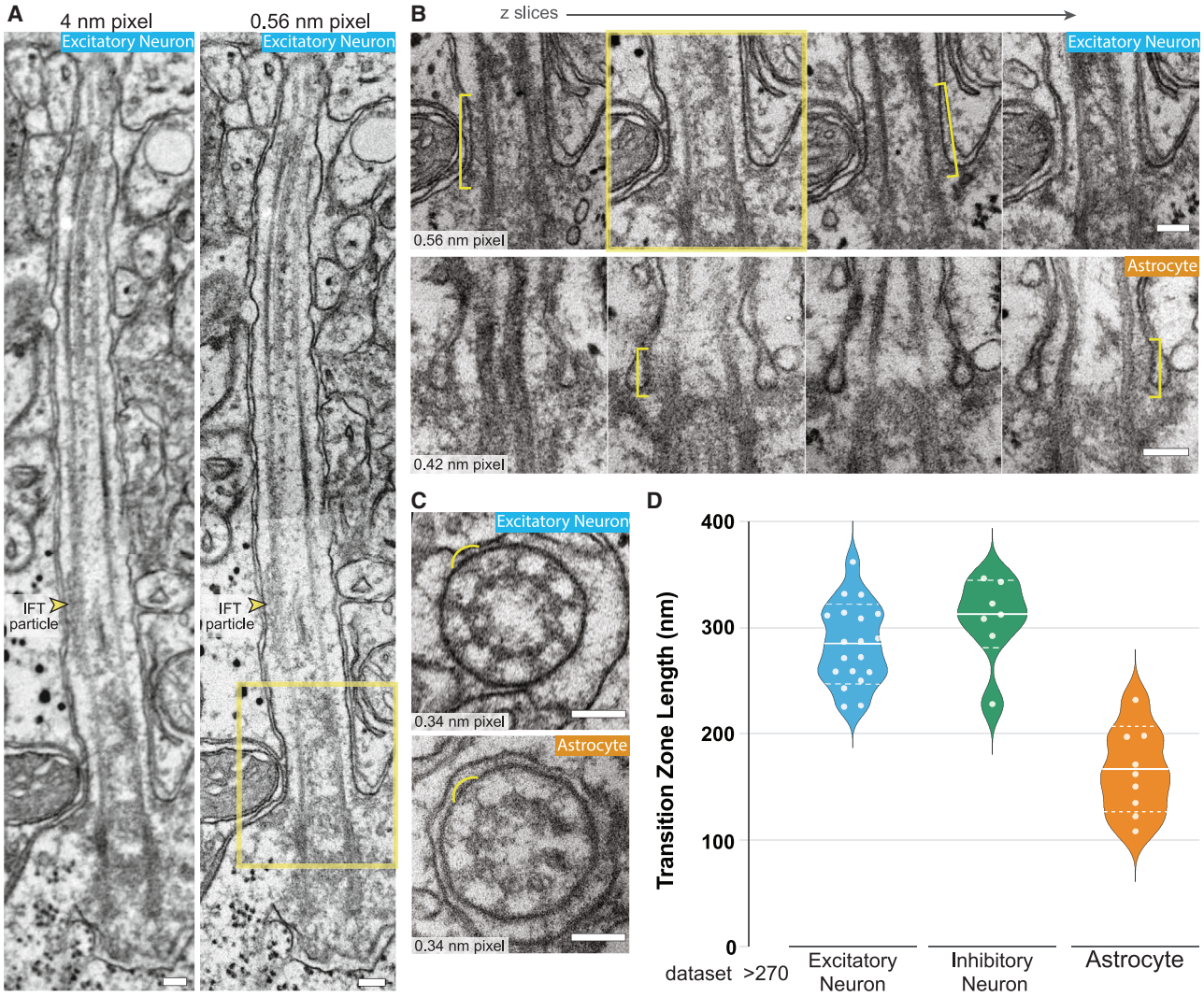

Figure 3. Astrocytic cilia TZs are shorter than neuronal cilia TZs

(A) To improve resolution, cilia from P>270 were located on the original EM grids and reimaged at higher resolutions (left, original; right, reimaged; yellow arrowhead, an IFT particle). Scale bars, 100 nm.

(B) Serial images of the base of an excitatory neuronal cilium and an astrocytic cilium (yellow bracket, TZ visible in alternating slices; yellow box, ROI in (A). Scale bars, 100 nm.

(C) The Y-links (yellow arcs) of the TZ are resolved in high-resolution images of excitatory neuronal and astrocytic cilia cross-sections. Scale bars, 100 nm.

(D) The distribution of mean TZ lengths measured in sequential images of lengthwise-sectioned cilia in P>270 is plotted (weighted mean, solid white line; dashed lines, standard deviation of the weighted mean).

See also Figure S3.

terminating microtubule suggested a capping or termination structure.

To investigate how internal changes in cilia microtubules affect overall cilia structure, we measured cilium diameter in 3D reconstructions. All cilia narrow within the first 4–5 μm in the region where microtubule transitions and termination happen (Figure 4D). The diameters of both inhibitory and excitatory neuronal cilia decreased steadily along the first 3 μm, however, astrocyte and OPC cilia diameters dropped off more quickly (Figure 4D; Video S2). OPC cilia diameter varied more, possibly caused by internal vesicles. Also, OPC cilia membranes constricted less uniformly as microtubules terminated (Figure S4E).

To investigate stereotyping of microtubule termination we examined cilia in the >P270 dataset and quantified singlets present at the most distal resolvable section (insufficient resolution and oblique cut angles prevented quantification in many cilia). We found all possible singlet configurations in distal cilia (Figure 4E). Plots of singlets near the terminus by cell type (Figure S4D) suggest that glial cilia were most likely to have only a few singlets near the tip.

Little is known about the function or prevalence of microtubule-associated proteins (MAPs) in brain cilia. We found densities tethering microtubules to the ciliary membrane or to each other (Figures 4B, S4B, and S4E). These densities could be

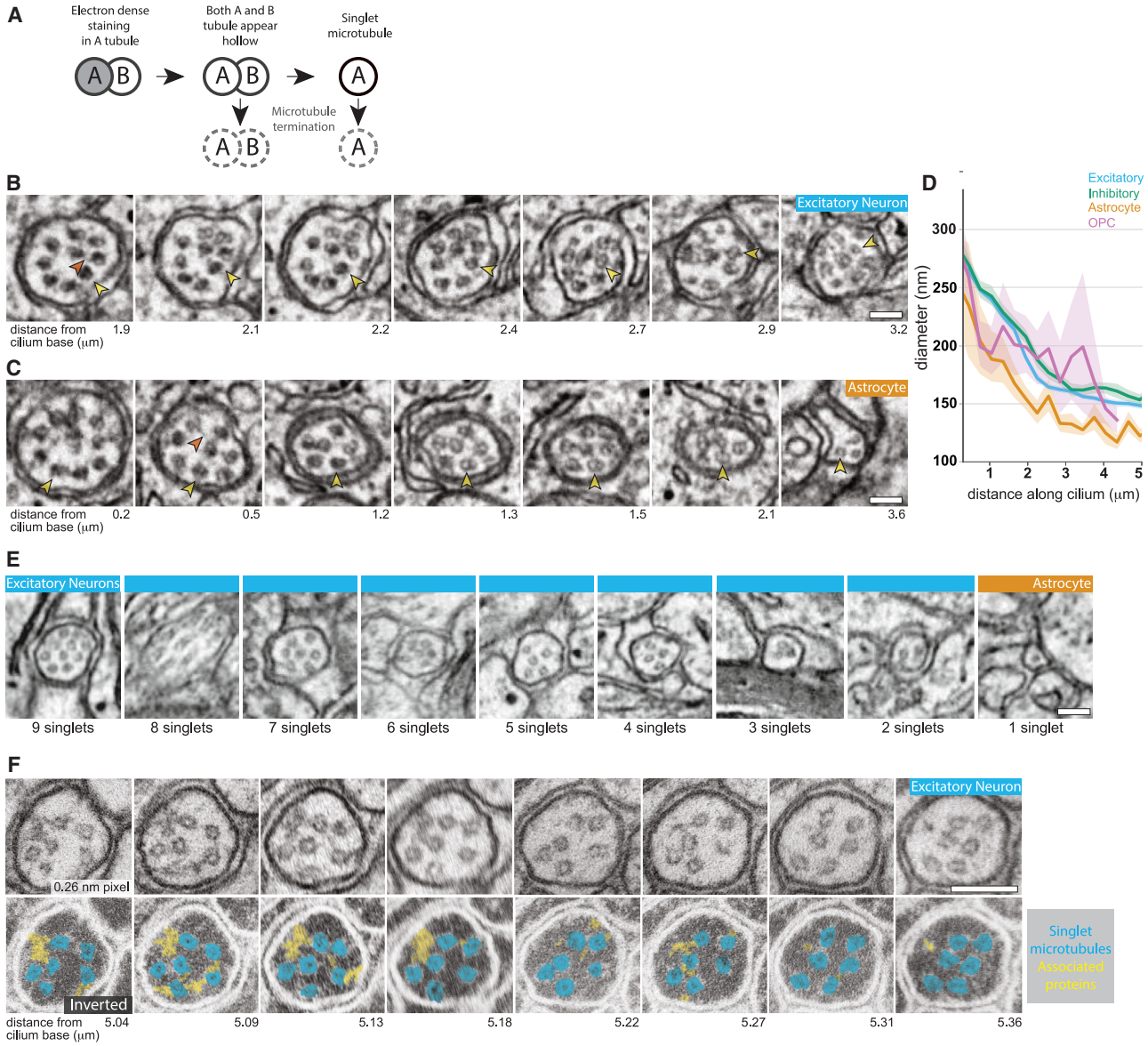

Figure 4. Astrocytic and neuronal cilia microtubule organization differs

(A) Microtubule transitions: microtubules emerge as doublets with A- and B-tubules. Density within the A-tubule ends leaving translucent lumens in both tubules. Some microtubules transition to singlets. Both doublet and singlet microtubules terminated.

(B and C) Cross-sections of an excitatory neuron (B) and an astrocytic cilium base (C). Yellow arrowheads track the position of the same microtubule through the volume. Orange arrowheads indicate densities between deviant microtubules and adjacent doublets. Scale bars, 100 nm.

(D) The diameter along the central path length of the proximal cilium was measured in P54 (solid lines: average diameter of a binned path length; shading: 95% CI of that bin).

(E) Cross-sections near tips of cilia display the diversity of microtubule configurations. Scale bars, 100 nm.

(F) Serial cross-sections of an excitatory neuron distal cilium re-imaged at higher resolution. Images were inverted in the lower panel (yellow: bridging electron densities; cyan: microtubules). Scale bars, 100 nm.

See also Figure S4 and Videos S2 and S3.

similar to those observed in kidney cilia and cultured epithelial cells.[51,52] We also observed previously unreported densities that connect the deviant microtubule to adjacent doublets (Figures 4B, S4B, and S4C). These bridging structures suggest that reorganization is accomplished through inter-doublet protein bridges. In reimaged cross-sections of the distal cilium (Figure 4F), bridging complexes associated with singlet microtubules. More research is needed to determine the identity and functions of MAPs in cilia.

Cilia project into a tangle of neurites and glial filaments

We expanded our investigation to the environment outside the cilium. Near the base, many cilia remained proximal to the cell body, while others projected directly into the neuropil.

CellPress
OPEN ACCESS

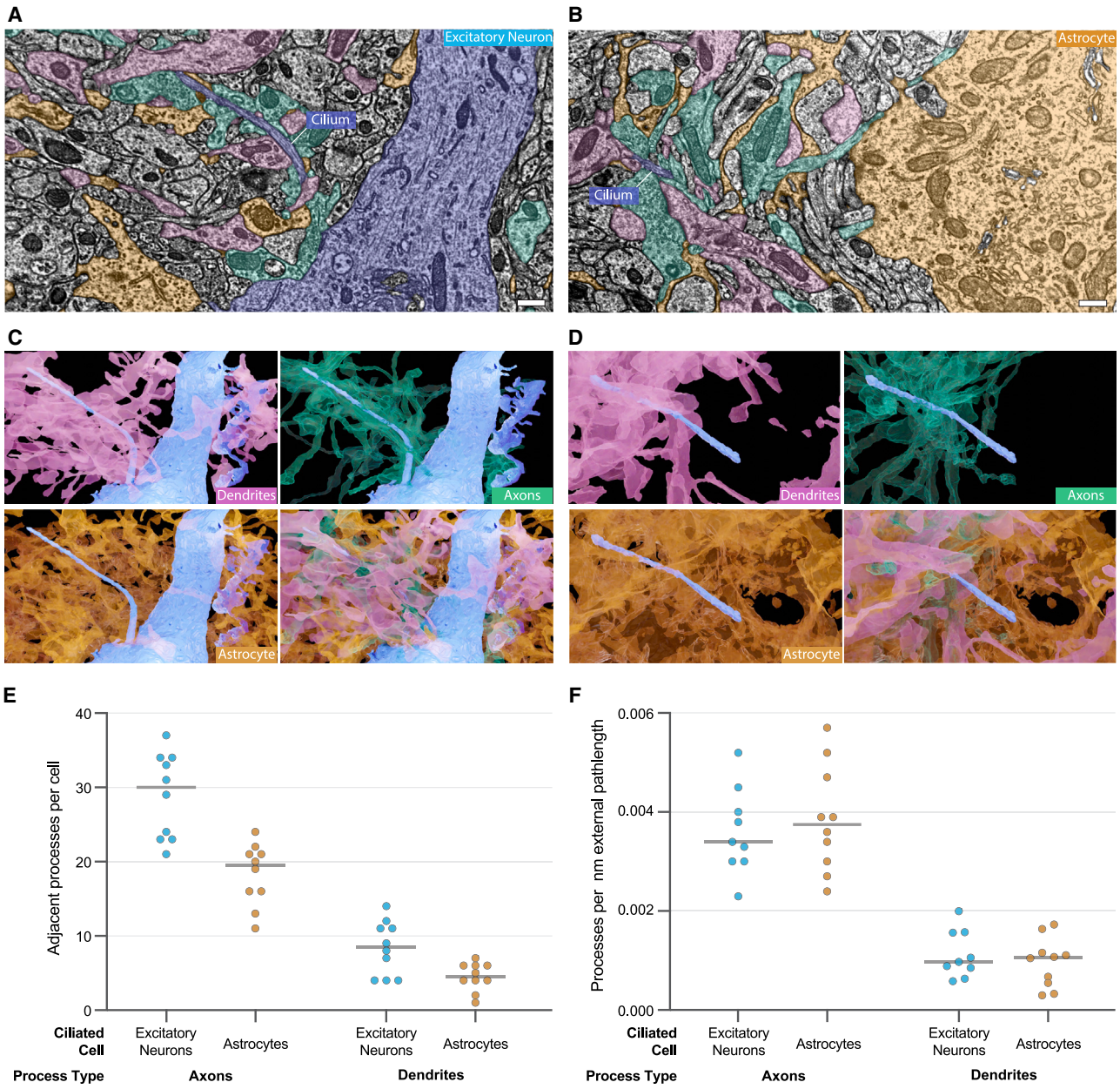

Figure 5. Cilia immersed in the neuropil

(A and B) Cilia on an excitatory neuron (A) or astrocyte (B) in P36 are shown in blue. Every process in the neuropil that passes adjacent to any portion of the cilium was colored by the processes' type (dendrites: pink; axons: teal; astrocyte: orange). Scale bars, 500 nm.

(C and D) 3D renderings of dendrites, axons, and astrocytic processes adjacent to each cilium from (A) and (B).

(E) Adjacent processes' identities were determined for 10 excitatory neurons and 10 astrocytes in P36 and the totals graphed.

(F) Process total from each cell was divided by its external cilium path length and graphed by cell class.

See also Figure S5 and Videos S3 and S4.

Figures 5A and 5B provide representative views of the complex extraciliary environment with processes shaded by type (see also Videos S3 and S4). To communicate the complexity of the cilium niche, we generated 3D renderings of cilia and the adjacent axons, dendrites, or glial processes (Figures 5C and 5D). Cilia were adjacent to astrocyte processes at several points along their length. Cilia tips were occasionally enveloped by astrocytes and in one case by a microglial process (Figure S5A). As expected because of astrocyte tiling,[55] the adjacent astrocyte processes were from only one or two cells. We quantified the number of axons and dendrites adjacent to 10 excitatory neuronal cilia and 10 astrocytic cilia in P36 (Figure 5E). Astrocytic cilia averaged fewer adjacent axons and dendrites than excitatory neuronal cilia. The portion of the astrocytic cilium shielded by the ciliary pocket has no adjacent processes (Figure 5D). To determine whether the ciliary pocket accounted for the observed

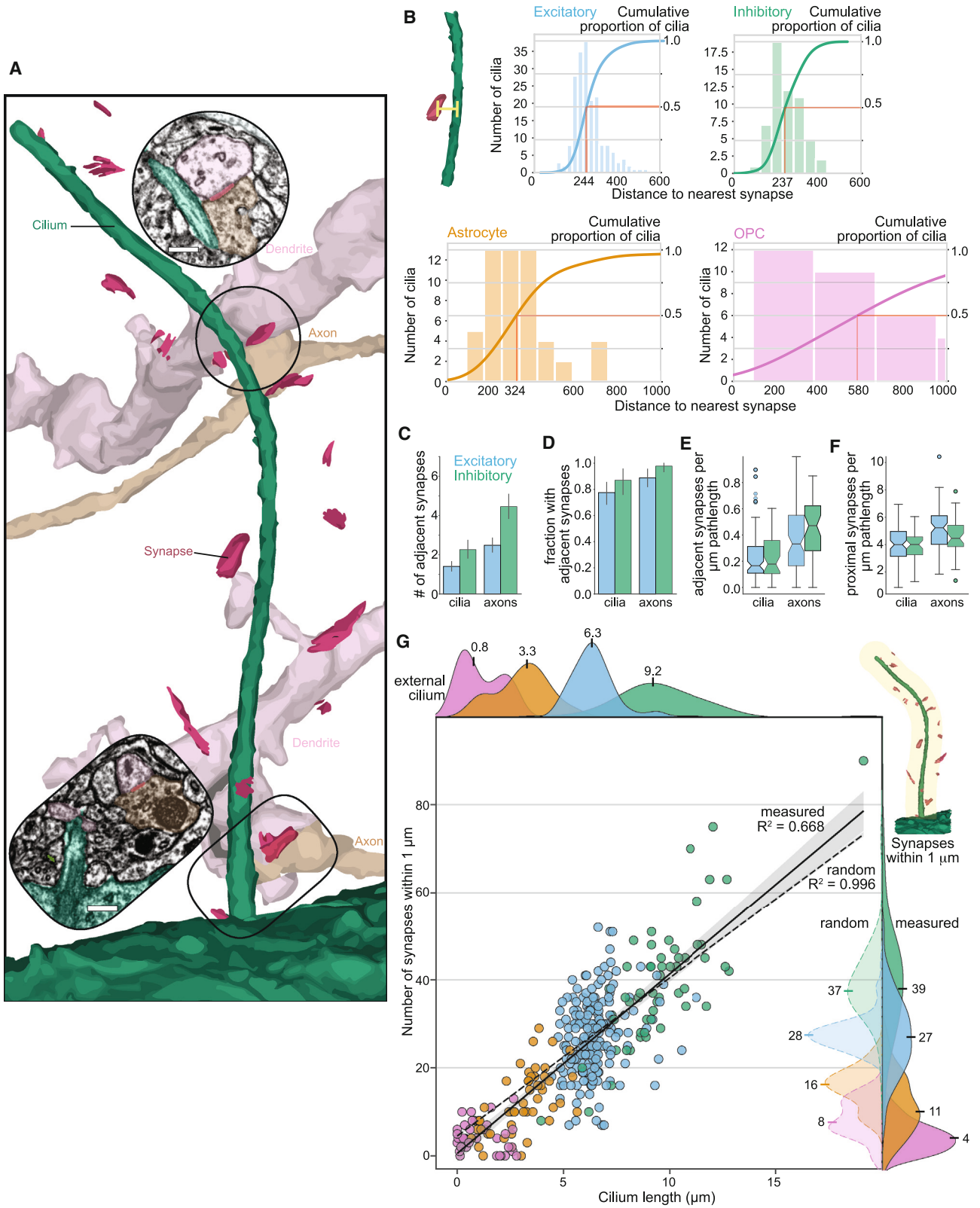

Figure 6. Cilium length and synapse abundance determined frequency of synapses near cilia

(A) Representative volumetric rendering of synapses near an inhibitory neuronal cilium (cilium, green; synaptic clefts, bright pink). Insets: EM images of an adjacent synapses (upper) and a proximal synapse (lower). Scale bars, 300 nm.

(legend continued on next page)

differences, we graphed the number of adjacent processes per nanometer external path length (Figure 5F) and found the mean values were more similar.

Neuronal processes near cilia could contain dense core vesicles (DCVs).[56] To investigate this possibility, we compared DCV proximity to cilia across cell classes by quantifying DCVs within 1 μm of the cilium center (Figures S5B and S5C). We then plotted the number of DCVs as a function of cilium length (Figure S5D). Astrocytic cilia had 10 or fewer DCVs within 1 μm, while neuronal cilia had more. DCVs were more frequently found in the region surrounding neuronal cilia, but we encountered a few DCVs poised to release peptides directly onto primary cilia.

Synapses were frequently found near and next to cilia

Receptors for neuromodulators, which can be released from clear synaptic vesicles, localize to neuronal cilia.[57] To investigate the possibility that locally released neuromodulators could reach primary cilia, we examined synapses near primary cilia. Both synapses directly adjacent to cilia (Figure 6A, upper inset, and Figures S6A and S6B) and proximal to cilia (Figure 6A, lower inset, and Figure S6B) could be within range of synaptic spillover if not shielded by perisynaptic astroglial processes.[58,59] Synapses were also recently found adjacent to cilia in an EM volume of the human anterior temporal lobe.[23] Sheu et al.[25] reported that axons can synapse directly onto cilia. In P36 and P54, synapses have been segmented and automatically connected to their pre- and post-synaptic reconstructions.[60] Although the automatic segmentation identified rare synapses onto cilia, these were false positives. Instead, all presynaptic termini had postsynaptic targets other than the cilium (i.e., axon-dendrite synapses, axon-axon synapses, and axon-soma synapses).

To assess synapse frequency near primary cilia, we measured the distance from each cilium to the center of the nearest synapse in P54 and plotted the distribution (left y axis, Figure 6B). Half of the excitatory neuronal cilia had a synapse within 244 nm. Inhibitory neurons were similar (237 nm), however, the average distance to the nearest synapse from astrocytic and OPC cilia was larger (324 and 580 nm, respectively). By measuring the distance to the nearest synapse, we determined that almost every neuron and astrocytic cilium had at least one synapse within 1 μm (right y axis, Figure 6B). For each cilium, we identified proximal synapses within 1 μm for further analysis.

Distinctiveness of synapse frequency near cilia was assessed in a human dataset by comparing the number of synapses adjacent to cilia to the number adjacent to a nearby axon of same neuron class.[23] To perform a similar comparison, we manually identified synapses adjacent to cilia and axons of 17–44 excitatory neurons from each layer and 55 inhibitory neurons in P54. In contrast to the measurements in the human temporal lobe,[23] on average we observed more synapses adjacent to axon segments than cilia (Figure 6C). Specifically, we found a mean of 1.5 ± 0.23 and 2.13 ± 0.44 synapses per cilium (95% CI; excitatory and inhibitory, respectively) (Figure 6C). 79.4% of excitatory cilia and 87.8% of excitatory axon fragments had at least one synapse adjacent and inhibitory values were higher (85.5% of cilia and 97.8% of axon fragments) (Figure 6D).

To determine whether higher synapse frequency was related to cilia length, we plotted the number of adjacent synapses (Figures 6E and S6C) or total synapses (Figure 6F) within 1 μm per unit path length for both cilia and axon fragments. This eliminated the differences between cell class seen in Figure 6C. Axons, however, did exhibit cell class distinctions in synapse adjacency, which suggest that they may not be a reliable benchmark. As axon fragments could not be class matched to glial cilia, we also calculated synapse frequency per unit path length within 1 μm of every glial and neuronal cilia in P54. Astrocytic and OPC cilia had lower averages (2.42 ± 0.38 and 1.46 ± 0.36 synapses per μm [95% CI], respectively) than excitatory and inhibitory neuronal cilia (4.28 ± 0.19 and 4.07 ± 0.26 synapses per μm [95% CI], respectively). However, when we calculated the synapse frequency per unit path length for just the external astrocytic cilia, the value increased (4.12 ±0.56 synapses per μm; 95% CI). Together, these data both support the hypothesis that the ciliary pocket limits exposure of the cilium and suggest that synapse density determines the frequency of synapse proximity.

We were concerned that comparisons to axon fragments were inadequate to evaluate whether the frequency of synapses near cilia was truly distinctive. Thus, we computationally placed the 3D mesh of each cilium from P54 in 1,000 random positions and orientations within the volume. We then determined the number of proximal synapses at each position and compared these results to the observed synapses (Figures 6G and S6D). For both excitatory and inhibitory neurons, the mean number of observed proximal synapses was similar to the values generated by random cilia placement (excitatory: 27 observed versus 28 random; inhibitory: 37 observed versus 39 random). In contrast, the external portion of astrocytic and OPC cilia had fewer observed proximal synapses than calculated with randomly placed cilia (observed means: 11 and 4; random means: 16 and 8, respectively). These data suggest that an additional factor might decrease glial cilia proximity to synapses. As an extension of this analysis, we also plotted the mean number of proximal synapses as a function of external cilium length. We

(B) Euclidean distance to the synapse closest to each cilium in P54 (left y axis: bar graph; bar width represents binning distances; right y axis: line shows cumulative fraction of cells that have a synapse within that distance; red line, half of cilia have a nearby synapse).
(C) The mean number of synapses adjacent to either cilia or axon fragments of equal length are graphed for both inhibitory and excitatory neurons.
(D) The fraction of cilia or axon fragments with adjacent synapses from (C) is graphed. Error bars in (C) and (D) represent 95% CI.
(E and F) The number of adjacent (E) or proximal (F) synapses divided by cilium/axon path length graphed using a box-and-whisker plot where the 95% CI is represented by the magnitude of the box indentation at the mean value. For (C)–(F), n = 89 excitatory cilia or excitatory axon fragments and 46 inhibitory cilia or axon fragments.
(G) The number of synapses within 1 μm of each P54 cilium graphed relative to external cilium length (solid line: linear regression fit across the dataset with β = 4.08, R^2 = 0.668; shading: 95% CI). Dashed line is the linear regression fit of the mean number of synapses adjacent to cilia randomly placed in 1,000 positions/orientations (β = 3.59 R^2 = 0.996, utilized external portion of cilia path). Top histogram: class distributions of cilia lengths. Right histograms: class distributions of the measured or calculated (random) synapses within 1 μm. OPCs, pink; astrocytes, orange; excitatory neurons, blue; inhibitory neurons, green.
See also Figure S6.

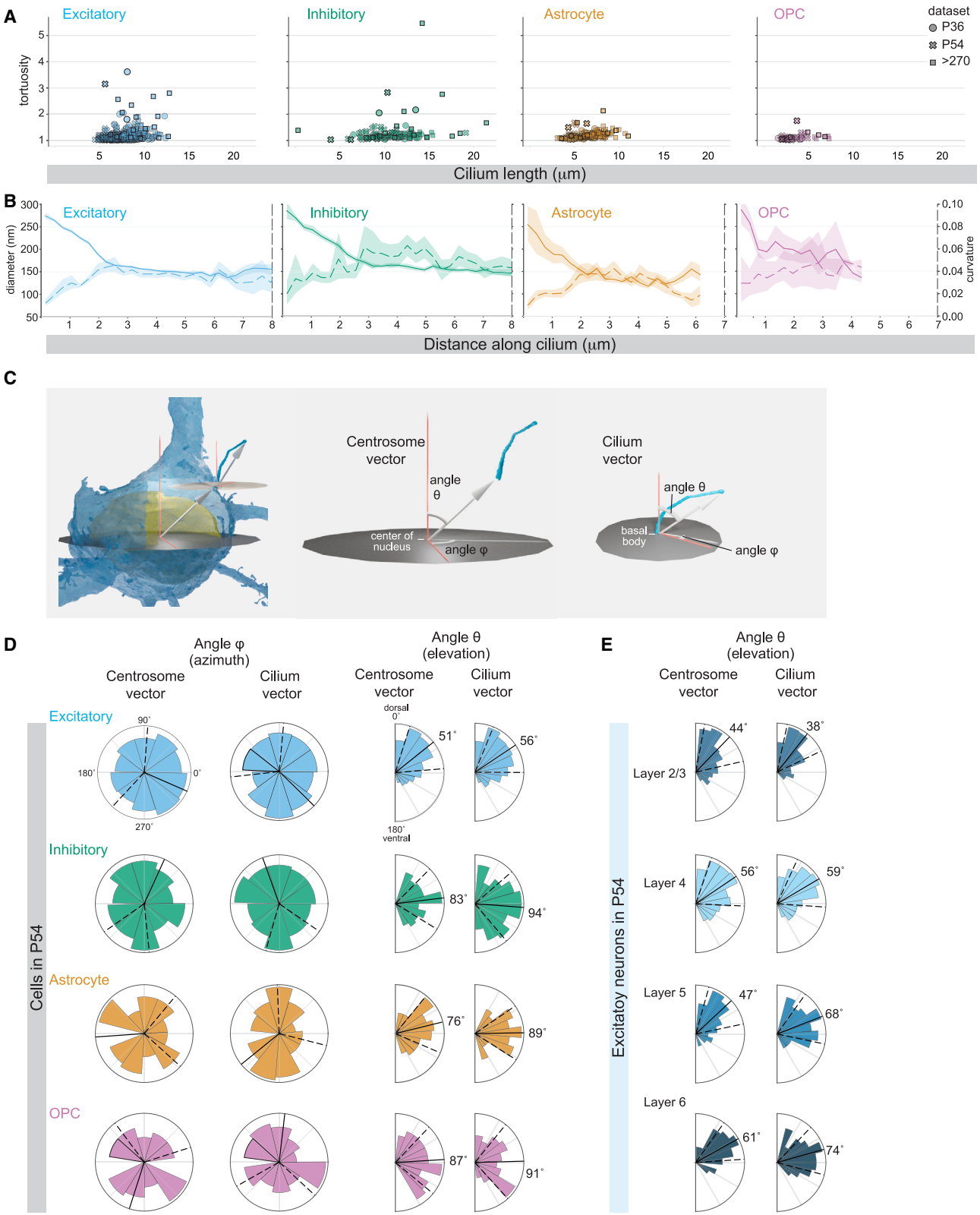

Figure 7. Cilium shape, placement, and orientation can be stereotyped within a cell class

(A) Gross tortuosity plotted relative to cilium length.

(B) Average cilium diameter in P54 (left y axis, solid line) and local curvature (right y axis, dashed line) along the cilium length. Shading indicates the 95% CI.

(legend continued on next page)

then compared the fit of the data and found that the observed proximal synapses fit a linear regression coefficient of 4.08 with R^2 = 0.668 (Figure 6G). This was similar to the coefficient derived from randomly distributed cilia (3.59, R^2 = 0.996) (Figures 6G and S6D) and less than the coefficient from analysis of synapses proximal to axon segments equal in length to cilia (coefficient = 4.55, R^2 = 0.387; Figure S6E). Because most glial cilia were partially submerged in a pocket, using the total path length for astrocytes and OPCs changed the coefficient value to 4.91 and decreased the R^2 to 0.606 (Figure S6E). We conclude that while glial cilia might be somewhat shielded, the number of synapses proximal to neuronal cilia was determined by cilium length and synapse abundance.

EM analysis reveals cell-class-specific features of cilia shape, placement, and orientation

Although similar, each segmented cilium mesh was unique (Figure S8). The physical properties of the cilium—its length, tortuosity, position, and orientation—could influence the exposure of the cilium to external ligands. We compared the overall tortuosity defined by arc-chord ratio of cilia and found that tortuosity across all cell classifications averaged 1.19 ± 0.02 (95% CI), close to the straight-line value of 1 (Figure 7A). Further, the gross tortuosity metric appeared unaffected by cilia length, indicating that the distal region with few singlet microtubules (and thus a decreased persistence length) did not bend more. Next, we investigated the relationship between cilium curvature and diameter by plotting the binned local curvature along the cilium length. On the same y axis, we also plotted cilium diameter (Figure 7B). The value of local curvature increased as the diameter decreased in neuronal and astrocytic cilia (Figure 7B) and both values leveled out at a similar distance from the base. Thus, the internal changes in microtubules correlated with both cilia diameter constriction and local curvature increase. The rate of local curvature appeared sustained in the distal cilium, preventing longer cilia from becoming increasingly tortuous. While OPC cilia diameter dropped close to the base, diameter stability and curvature leveling were not apparent (possibly related to the internal vesicles in Figure S2).

Finally, we examined cell class similarities in centriole placement and cilium orientation. There is evidence that cilia within populations of neurons can align.[23,24,61] To investigate centriole positioning and cilia orientation we used two vectors: (1) the centrosome vector, which defined the cilium origin, extended from the center of the nucleus to the mother centriole; and (2) the cilium vector, which defined cilium orientation, extended from the base of the cilium to the tip (Figure 7C). For each vector, we plotted the angle phi (the direction of the vector angle relative to the rostral-caudal and anterior-posterior axis) and the angle theta (elevation or depression toward or away from the pia, i.e., dorsal or ventral) (Figure 7D). Phi was distributed throughout the possible angles for all cell classes. In contrast, both excitatory neuron centrosome and cilia vector theta values condensed around an average of 51° and 56°, respectively. In P36 excitatory neurons, the values were similar (centrosome theta: 46°; cilia theta: 50). The polarized centriole vector meant that the mother centrioles docked near the base of the apical dendrite. The polarized cilia vector meant that, on average, cilia oriented toward the pia. We compared the cilia and centrosome vectors between cells of the same class at different depths (Figure 7E). The positioning of the cilium origin and the directionality of the cilium vector shifted away from the zenith (for example, the cilium vector shifted from 38° in layer 2/3 to 74° in layer 6). Taken together, the analysis of the physical properties of cilia revealed that centrosomes and axoneme microtubules (interior structures) influenced the shape and trajectory of cilia, which in turn affected cilium exposure in the neuropil.

DISCUSSION

Analysis of volumetric EM datasets revealed cell-type-specific differences in cilia ultrastructure. Cilia differed in length, origin structure, TZ length, microtubule organization, and the presence of internal vesicles. These features influenced placement in the 3D environment outside cilia—the context for signal transmission and detection. Together with quantitative analysis of primary cilia position and orientation, we have a new understanding of how cell-specific structural features could determine cilia exposure to external signals.

Ultrastructural differences may be a consequence of biogenesis and could reflect functional differences. For example, the sub-population of astrocytes that had surface cilia could be functionally distinct. The division between pocket cilia and surface cilia may reflect different ciliogenesis pathways. In the visual cortex, neurons overwhelmingly had surface cilia, but that is not true of all neurons.[23,62] In the mouse optic nerve, astrocytes had concealed or pocket cilia and OPCs had surface cilia.[63] The differences between neuronal and astrocytic TZs may differ in other brain regions and TZs might change over time, as seen in other systems.[48,49] In *Drosophila*, the immotile cilia of olfactory neurons and the motile cilia in auditory neurons have different Y-link structures.[50] We speculate that previously unrecognized structural differences between cell types could explain why mutation of genes coding for cilia and centrosome proteins can have diverse disease outcomes.

Recent cilia studies using EM volumes lacked the contrast and resolution necessary for detailed comparisons of axoneme microtubules and associated proteins.[23,24] Differences between neuronal and glial axoneme microtubules could be caused by expression of different tubulin monomers.[64] Recent investigations revealed that a mutation in the beta tubulin isotype Tubb4b disrupts axoneme formation and stability.[65] If the A tubule

(C) The centrosome vector originates at the center of the nucleus and extends to the mother centriole. The cilium vector extends from the base of the cilium to the tip. The azimuth is represented by the angle φ and the elevation by the angle θ. The spherical coordinate system is defined by a zenith representing an axis from white matter to pia.
(D) Polar plots show the distribution of centrosome and cilia vectors for each cell in each class in P54 (solid black line: the circular mean; dashed lines: the circular standard deviation around the mean).
(E) Centrosome and cilium vectors of excitatory neurons in each layer.
See also Figure S7.

staining represented MIPs, their presence may prevent B-tubule termination. The observed configurations of doublet and singlet microtubules revealed gaps in our knowledge about intraflagellar transport (IFT), which has been shown to be tubule-dependent in motile cilia (anterograde transport on the B-tubule and retrograde transport on the A-tubule).[66] In *C. elegans*, alternate motor configurations conduct anterograde transport on distal microtubule singlets.[67] The issue of IFT in the absence of B-tubules, has been raised by Sun et al.[51] Based on serial section electron tomography of cultured epithelial cell cilia, they also predict that microtubules bridging densities are MAPs. Microtubules, MIPS, and MAPS may contribute to both stability and dynamism as cilia change through development and through a single day.[21,22,68]

Abundant axons, dendrites, and glial processes surrounding cilia suggested novel influences on cilia signaling. The prevailing paradigm—that peptide signaling occurs largely through bulk flow—is consistent with our observations; however, automated identification of DCVs would facilitate a more comprehensive analysis. Glycoproteins, which facilitate cilia adhesion in cultured cells,[69] may also facilitate cilia adhesion to adjacent processes. Gap junctions were proposed to link cilia to processes in the human temporal lobe.[23] In the visual cortex, we found no high confidence gap junctions. Automated identification, EM-dense labeling, or datasets with higher resolution will be necessary to demonstrate that gap junctions impact cilia function.

We hypothesize that ciliary membrane receptors for synapse-released neuromodulators detect ligands able to travel a short distance from the synapse. In addition to cilia-localized serotonin and dopamine receptors, metabotropic neurotransmitter receptors could also localize to cilia.[70] As spillover is known to activate extrasynaptic receptors,[71] and neurotransmitter diffusion in cultured slices can travel more than 1 μm,[72] cilia could detect molecules released from both proximal and adjacent synapses. In addition, signals released from multiple synapses could be integrated sequentially or simultaneously.

While our analysis had much in common with related studies, we draw different conclusions on three aspects of synapse-mediated signaling. First, we found that the number of proximal synapses was determined by local synapse density and cilium length. This deviates from the conclusion that synapses preferentially associate with cilia based on comparison to synapse adjacency to axonal fragments.[23] Brain-region or species differences in the nature and abundance of synapses between the mouse and human cortex[73] could contribute to this disparity in mean adjacent synapses. However, as synapses are abundant in both, the distinction may be near axons. Second, we draw no conclusions regarding tetrapartite synapses, where both cilia and astrocytes are adjacent to a synaptic cleft. At tripartite synapses, astrocytic processes both receive and modulate synaptic transmission.[74,75] As there is no evidence that cilia modulate synaptic release, we hypothesize that cilia passively detect diffusing molecules; thus, labeling structures as tetrapartite synapses is premature and potentially misleading. Third, we observed no synapses directly onto cilia: all presynaptic termini near primary cilia had a separate post-synaptic target.

We are just beginning to understand how primary cilia influence neuronal and glial activity.[76,77] This ultrastructural analysis demonstrated that primary cilia are not all the same and that some features, like ciliary pockets or glial processes might shield cilia from potential ligands, while others, especially synapses, could be signaling sources. In combination with placement of the cilium origin, regulation of cilia structural features determined the extracellular environment monitored by cilia localized receptors.

STAR★METHODS

Detailed methods are provided in the online version of this paper and include the following:

- KEY RESOURCES TABLE
- RESOURCE AVAILABILITY
  - Lead contact
  - Materials availability
  - Data and code availability
- EXPERIMENTAL MODEL AND STUDY PARTICIPANT DETAILS
  - Overview of TEM datasets
- METHOD DETAILS
  - Cell classifications
  - Annotation of cilia and centrosomes
  - Annotation postprocessing
  - Manual segmentation in Amira
  - Re-imaging TEM sections at higher resolution
  - Visualization of 3D objects using Blender 3.1.2
  - Skeleton generation and processing
- QUANTIFICATION AND STATISTICAL ANALYSIS
  - Transition zone measurements
  - Quantification of processes adjacent to cilia
  - Quantification of dense core vesicles near cilia
  - Synapse data analysis
  - Orientation calculations
  - Morphological calculations

SUPPLEMENTAL INFORMATION

Supplemental information can be found online at https://doi.org/10.1016/j.cub.2024.04.043.

ACKNOWLEDGMENTS

C.M.O., D.D.B., and J.L.-S. were supported by the Howard Hughes Medical Institute. N.M.d.C. and D.D.B. acknowledge support from NSF NeuroNex 2 award 2014862. W.C.L. acknowledges support from the NIH (MH117808). We thank Tom Kazimiers from kazmos GmbH for open-source CATMAID code and managing the CATMAID instance. We also thank Jennifer Garrison and the Les Treilles Foundation for bringing collaborators together. Janet Iwasa helped with early visualizations of cilia microtubules, and we used Andrew Price's Blender tutorials. We also thank Christina Gladkova, Lauren Porter, Andy Moore, Chris Obara, Casey Schneider-Mizell, Tess Oram, Saikat Mukhopadhyay, and Cayla Jewett for helpful discussions and comments on the manuscript. We thank the Allen Institute for Brain Science founder, Paul G. Allen, for his vision, encouragement, and support.

AUTHOR CONTRIBUTIONS

C.M.O., R.T., N.M.d.C., and J.L.-S. conceived the project and wrote the paper with input from all authors. C.M.O. annotated and analyzed EM data. C.M.O. and R.T. analyzed the data. T.-S.K. located and re-imaged sections with help from W.C.L and A.K., who also processed and aligned images. D.D.B. helped with early annotation of the P>270 dataset and J.B., L.E., S.S., A.L.B., F.C., D.D.B., C.M.O., and N.M.d.C. provided cell identification and classification.

DECLARATION OF INTERESTS

The authors have no competing financial interests to declare.

Received: November 6, 2023
Revised: March 27, 2024
Accepted: April 22, 2024
Published: May 14, 2024

REFERENCES

1. Allen, R.A. (1965). Isolated cilia in inner retinal neurons and in retinal pigment epithelium. J. Ultrastruct. Res. *12*, 730–747. https://doi.org/10.1016/s0022-5320(65)80058-2.
2. Barnes, B.G. (1961). Ciliated secretory cells in the pars distalis of the mouse hypophysis. J. Ultrastruct. Res. *5*, 453–467. https://doi.org/10.1016/s0022-5320(61)80019-1.
3. Higginbotham, H., Eom, T.-Y., Mariani, L.E., Bachleda, A., Hirt, J., Gukassyan, V., Cusack, C.L., Lai, C., Caspary, T., and Anton, E.S. (2012). Arl13b in Primary Cilia Regulates the Migration and Placement of Interneurons in the Developing Cerebral Cortex. Dev. Cell *23*, 925–938. https://doi.org/10.1016/j.devcel.2012.09.019.
4. Higginbotham, H., Guo, J., Yokota, Y., Umberger, N.L., Su, C.-Y., Li, J., Verma, N., Hirt, J., Ghukasyan, V., Caspary, T., and Anton, E.S. (2013). Arl13b-regulated cilia activities are essential for polarized radial glial scaffold formation. Nat. Neurosci. *16*, 1000–1007. https://doi.org/10.1038/nn.3451.
5. Koemeter-Cox, A.I., Sherwood, T.W., Green, J.A., Steiner, R.A., Berbari, N.F., Yoder, B.K., Kauffman, A.S., Monsma, P.C., Brown, A., Askwith, C.C., and Mykytyn, K. (2014). Primary cilia enhance kisspeptin receptor signaling on gonadotropin-releasing hormone neurons. Proc. Natl. Acad. Sci. USA *111*, 10335–10340. https://doi.org/10.1073/pnas.1403286111.
6. Tong, C.K., Han, Y.-G., Shah, J.K., Obernier, K., Guinto, C.D., and Alvarez-Buylla, A. (2014). Primary cilia are required in a unique subpopulation of neural progenitors. Proc. Natl. Acad. Sci. USA *111*, 12438–12443. https://doi.org/10.1073/pnas.1321425111.
7. Vien, T.N., Ta, M.C., Kimura, L.F., Onay, T., and DeCaen, P.G. (2023). Primary cilia TRP channel regulates hippocampal excitability. Proc. Natl. Acad. Sci. USA *120*, e2219686120. https://doi.org/10.1073/pnas.2219686120.
8. Guo, J., Otis, J.M., Suciu, S.K., Catalano, C., Xing, L., Constable, S., Wachten, D., Gupton, S., Lee, J., Lee, A., et al. (2019). Primary Cilia Signaling Promotes Axonal Tract Development and Is Disrupted in Joubert Syndrome-Related Disorders Models. Dev. Cell *51*, 759–774.e5. https://doi.org/10.1016/j.devcel.2019.11.005.
9. Davenport, J.R., Watts, A.J., Roper, V.C., Croyle, M.J., van Groen, T., Wyss, J.M., Nagy, T.R., Kesterson, R.A., and Yoder, B.K. (2007). Disruption of intraflagellar transport in adult mice leads to obesity and slow-onset cystic kidney disease. Curr. Biol. *17*, 1586–1594. https://doi.org/10.1016/j.cub.2007.08.034.
10. Valente, E.M., Rosti, R.O., Gibbs, E., and Gleeson, J.G. (2014). Primary cilia in neurodevelopmental disorders. Nat. Rev. Neurol. *10*, 27–36. https://doi.org/10.1038/nrneurol.2013.247.
11. Ma, R., Kutchy, N.A., Chen, L., Meigs, D.D., and Hu, G. (2022). Primary cilia and ciliary signaling pathways in aging and age-related brain disorders. Neurobiol. Dis. *163*, 105607. https://doi.org/10.1016/j.nbd.2021.105607.
12. Pruski, M., and Lang, B. (2019). Primary Cilia–An Underexplored Topic in Major Mental Illness. Front. Psychiatry *10*, 104. https://doi.org/10.3389/fpsyt.2019.00104.
13. Park, K., and Leroux, M.R. (2022). Composition, organization and mechanisms of the transition zone, a gate for the cilium. EMBO Rep. *23*, e55420. https://doi.org/10.15252/embr.202255420.
14. Soares, H., Carmona, B., Nolasco, S., Viseu Melo, L.V., and Gonçalves, J. (2019). Cilia Distal Domain: Diversity in Evolutionarily Conserved Structures. Cells *8*, 160. https://doi.org/10.3390/cells8020160.
15. Doroquez, D.B., Berciu, C., Anderson, J.R., SenGupta, P., and Nicastro, D. (2014). A high-resolution morphological and ultrastructural map of anterior sensory cilia and glia in Caenorhabditis elegans. eLife *3*, e01948. https://doi.org/10.7554/eLife.01948.
16. Kiesel, P., Alvarez Viar, G.A., Tsoy, N., Maraspini, R., Gorilak, P., Varga, V., Honigmann, A., and Pigino, G. (2020). The molecular structure of mammalian primary cilia revealed by cryo-electron tomography. Nat. Struct. Mol. Biol. *27*, 1115–1124. https://doi.org/10.1038/s41594-020-0507-4.
17. Klena, N., and Pigino, G. (2022). Structural Biology of Cilia and Intraflagellar Transport. Annu. Rev. Cell Dev. Biol. *38*, 103–123. https://doi.org/10.1146/annurev-cellbio-120219-034238.
18. Dahl, H.A. (1963). Fine structure of cilia in rat cerebral cortex. Z. Zellforsch. Mikrosk. Anat. (Vienna, Austria) *60*, 369–386. https://doi.org/10.1007/BF00336612.
19. Herman, M.M., Rubinstein, L.J., and McKhann, G.M. (1971). Additional electron microscopic observations on two cases of Batten-Spielmeyer-Vogt disease. (Neuronal ceroid-lipofuscinosis). Acta Neuropathol. *17*, 85–102. https://doi.org/10.1007/BF00687485.
20. Spacek, J. (1985). Solitary cilia of nerve and glial cells. Sbornik vedeckych praci Lekarske fakulty Karlovy univerzity v Hradci Kralove. Sb. Ved. Pr. Lek. Fak. Karlovy Univerzity Hradci Kralove Suppl. *28*, 443–451.
21. Ott, C.M., Constable, S., Nguyen, T.M., White, K., Lee, W.A., Lippincott-Schwartz, J., and Mukhopadhyay, S. (2023). Permanent deconstruction of intracellular primary cilia in differentiating granule cell neurons. Preprint at bioRxiv. https://doi.org/10.1101/2023.12.07.565988.
22. Constable, S., Ott, C.M., Lemire, A.L., White, K., Lim, A., Lippincott-Schwartz, J., and Mukhopadhyay, S. (2023). Programmed withdrawal of cilia maintenance followed by centriole capping leads to permanent cilia loss during cerebellar granule cell neurogenesis. Preprint at bioRxiv. https://doi.org/10.1101/2023.12.07.565993.
23. Wu, J.Y., Cho, S.-J., Descant, K., Li, P.H., Shapson-Coe, A., Januszewski, M., Berger, D.R., Meyer, C., Casingal, C., Huda, A., et al. (2024). Mapping of neuronal and glial primary cilia contactome and connectome in the human cerebral cortex. Neuron *112*, 41–55.e3. https://doi.org/10.1016/j.neuron.2023.09.032.
24. Sheu, S.-H., Upadhyayula, S., Dupuy, V., Pang, S., Deng, F., Wan, J., Walpita, D., Pasolli, H.A., Houser, J., Sanchez-Martinez, S., et al. (2022). A serotonergic axon-cilium synapse drives nuclear signaling to alter chromatin accessibility. Cell *185*, 3390–3407.e18. https://doi.org/10.1016/j.cell.2022.07.026.
25. Bock, D.D., Lee, W.-C.A., Kerlin, A.M., Andermann, M.L., Hood, G., Wetzel, A.W., Yurgenson, S., Soucy, E.R., Kim, H.S., and Reid, R.C. (2011). Network anatomy and in vivo physiology of visual cortical neurons. Nature *471*, 177–182. https://doi.org/10.1038/nature09802.
26. Schneider-Mizell, C.M., Bodor, A.L., Collman, F., Brittain, D., Bleckert, A., Dorkenwald, S., Turner, N.L., Macrina, T., Lee, K., Lu, R., et al. (2021). Structure and function of axo-axonic inhibition. eLife *10*, e73783. https://doi.org/10.7554/eLife.73783.
27. Dorkenwald, S., Turner, N.L., Macrina, T., Lee, K., Lu, R., Wu, J., Bodor, A.L., Bleckert, A.A., Brittain, D., Kemnitz, N., et al. (2022). Binary and analog variation of synapses between cortical pyramidal neurons. eLife *11*, e76120. https://doi.org/10.7554/eLife.76120.
28. Turner, N.L., Macrina, T., Bae, J.A., Yang, R., Wilson, A.M., Schneider-Mizell, C., Lee, K., Lu, R., Wu, J., Bodor, A.L., et al. (2022). Reconstruction of neocortex: organelles, compartments, cells, circuits, and activity. Cell *185*, 1082–1100.e24. https://doi.org/10.1016/j.cell.2022.01.023.
29. Buchanan, J., Elabbady, L., Collman, F., Jorstad, N.L., Bakken, T.E., Ott, C., Glatzer, J., Bleckert, A.A., Bodor, A.L., Brittain, D., et al. (2022). Oligodendrocyte precursor cells ingest axons in the mouse neocortex. Proc. Natl. Acad. Sci. USA *119*, e2202580119. https://doi.org/10.1073/pnas.2202580119.
30. Elabbady, L., Seshamani, S., Mu, S., Mahalingam, G., Schneider-Mizell, C., Bodor, A., Bae, J.A., Brittain, D., Buchanan, J., Bumbarger, D.J., et al. (2022). Quantitative Census of Local Somatic Features in Mouse

Visual Cortex. Preprint at bioRxiv. https://doi.org/10.1101/2022.07.20.499976.

31. Dorkenwald, S., Schneider-Mizell, C., and Collman, F. (2020). sdorkenw/MeshParty. Zenodo. https://doi.org/10.5281/zenodo.3710398.
32. Schneider-Mizell, C.M., Gerhard, S., Longair, M., Kazimiers, T., Li, F., Zwart, M.F., Champion, A., Midgley, F.M., Fetter, R.D., Saalfeld, S., et al. (2016). Quantitative neuroanatomy for connectomics in Drosophila. eLife *5*, e12059. https://doi.org/10.7554/eLife.12059.
33. Sipos, É., Komoly, S., and Ács, P. (2018). Quantitative Comparison of Primary Cilia Marker Expression and Length in the Mouse Brain. J. Mol. Neurosci. *64*, 397–409. https://doi.org/10.1007/s12031-018-1036-z.
34. Falcón-Urrutia, P., Carrasco, C.M., Lois, P., Palma, V., and Roth, A.D. (2015). Shh Signaling through the Primary Cilium Modulates Rat Oligodendrocyte Differentiation. Plos One *10*, e0133567. https://doi.org/10.1371/journal.pone.0133567.
35. Bear, R.M., and Caspary, T. (2024). Uncovering cilia function in glial development. Ann. Hum. Genet. *88*, 27–44. https://doi.org/10.1111/ahg.12519.
36. Kim, Y., Yang, G.R., Pradhan, K., Venkataraju, K.U., Bota, M., del García Del Molino, L.C.G., Fitzgerald, G., Ram, K., He, M., Levine, J.M., et al. (2017). Brain-wide Maps Reveal Stereotyped Cell-Type-Based Cortical Architecture and Subcortical Sexual Dimorphism. Cell *171*, 456–469.e22. https://doi.org/10.1016/j.cell.2017.09.020.
37. Zhao, H., Khan, Z., and Westlake, C.J. (2023). Ciliogenesis membrane dynamics and organization. Semin. Cell Dev. Biol. *133*, 20–31. https://doi.org/10.1016/j.semcdb.2022.03.021.
38. Sorokin, S.P. (1968). Reconstructions of centriole formation and ciliogenesis in mammalian lungs. J. Cell Sci. *3*, 207–230. https://doi.org/10.1242/jcs.3.2.207.
39. Molla-Herman, A., Ghossoub, R., Blisnick, T., Meunier, A., Serres, C., Silbermann, F., Emmerson, C., Romeo, K., Bourdoncle, P., Schmitt, A., et al. (2010). The ciliary pocket: an endocytic membrane domain at the base of primary and motile cilia. J. Cell Sci. *123*, 1785–1795. https://doi.org/10.1242/jcs.059519.
40. Rivera-Molina, F.E., Xi, Z., Reales, E., Wang, B., and Toomre, D. (2021). Exocyst complex mediates recycling of internal cilia. Curr. Biol. *31*, 5580–5589.e5. https://doi.org/10.1016/j.cub.2021.09.067.
41. Arellano, J.I., Guadiana, S.M., Breunig, J.J., Rakic, P., and Sarkisian, M.R. (2012). Development and distribution of neuronal cilia in mouse neocortex. J. Comp. Neurol. *520*, 848–873. https://doi.org/10.1002/cne.22793.
42. Reese, T.S. (1965). OLFACTORY CILIA IN THE FROG. J. Cell Biol. *25*, 209–230. https://doi.org/10.1083/jcb.25.2.209.
43. Banks, G., Lassi, G., Hoerder-Suabedissen, A., Tinarelli, F., Simon, M.M., Wilcox, A., Lau, P., Lawson, T.N., Johnson, S., Rutman, A., et al. (2018). A missense mutation in Katnal1 underlies behavioural, neurological and ciliary anomalies. Mol. Psychiatry *23*, 713–722. https://doi.org/10.1038/mp.2017.54.
44. Wakefield, S., and Waite, D. (1980). Abnormal cilia in Polynesians with bronchiectasis. Am. Rev. Respir. Dis. *121*, 1003–1010. https://doi.org/10.1164/arrd.1980.121.6.1003.
45. Shah, A.S., Farmen, S.L., Moninger, T.O., Businga, T.R., Andrews, M.P., Bugge, K., Searby, C.C., Nishimura, D., Brogden, K.A., Kline, J.N., et al. (2008). Loss of Bardet–Biedl syndrome proteins alters the morphology and function of motile cilia in airway epithelia. Proc. Natl. Acad. Sci. USA *105*, 3380–3385. https://doi.org/10.1073/pnas.0712327105.
46. Ruba, A., Tingey, M., Luo, W., Yu, J., Evangelou, A., Higgins, R., Khim, S., and Yang, W. (2023). The ciliary lumen accommodates passive diffusion and vesicle-assisted trafficking in cytoplasm–ciliary transport. Mol. Biol. Cell *34*, ar59. https://doi.org/10.1091/mbc.E22-10-0452.
47. Gilula, N.B., and Satir, P. (1972). The ciliary necklace. A ciliary membrane specialization. J. Cell Biol. *53*, 494–509. https://doi.org/10.1083/jcb.53.2.494.
48. Wiegering, A., Dildrop, R., Kalfhues, L., Spychala, A., Kuschel, S., Lier, J.M., Zobel, T., Dahmen, S., Leu, T., Struchtrup, A., et al. (2018). Cell type-specific regulation of ciliary transition zone assembly in vertebrates. EMBO J. *37*, https://doi.org/10.15252/embj.201797791.
49. Akella, J.S., Silva, M., Morsci, N.S., Nguyen, K.C., Rice, W.J., Hall, D.H., and Barr, M.M. (2019). Cell type-specific structural plasticity of the ciliary transition zone in C. elegans. Biol. Cell *111*, 95–107. https://doi.org/10.1111/boc.201800042.
50. Jana, S.C., Mendonça, S., Machado, P., Werner, S., Rocha, J., Pereira, A., Maiato, H., and Bettencourt-Dias, M. (2018). Differential regulation of transition zone and centriole proteins contributes to ciliary base diversity. Nat. Cell Biol. *20*, 928–941. https://doi.org/10.1038/s41556-018-0132-1.
51. Sun, S., Fisher, R.L., Bowser, S.S., Pentecost, B.T., and Sui, H. (2019). Three-dimensional architecture of epithelial primary cilia. Proc. Natl. Acad. Sci. USA *116*, 9370–9379. https://doi.org/10.1073/pnas.1821064116.
52. Gluenz, E., Höög, J.L., Smith, A.E., Dawe, H.R., Shaw, M.K., and Gull, K. (2010). Beyond 9+0: noncanonical axoneme structures characterize sensory cilia from protists to humans. FASEB J. *24*, 3117–3121. https://doi.org/10.1096/fj.09-151381.
53. Ma, M., Stoyanova, M., Rademacher, G., Dutcher, S.K., Brown, A., and Zhang, R. (2019). Structure of the Decorated Ciliary Doublet Microtubule. Cell *179*, 909–922.e12. https://doi.org/10.1016/j.cell.2019.09.030.
54. Ichikawa, M., Khalifa, A.A., Basu, K., Dai, D., Maghrebi, M.A.F., Vargas, J., and Bui, K.H. (2019). Tubulin Lattice in Cilia is in a Stressed Form Regulated by Microtubule Inner Proteins. Proc. Natl. Acad. Sci. USA *116*, 19930–19938. https://doi.org/10.1073/pnas.1911119116.
55. Baldwin, K.T., Murai, K.K., and Khakh, B.S. (2023). Astrocyte morphology. Trends Cell Biol. https://doi.org/10.1016/j.tcb.2023.09.006.
56. van den Pol, A.N. (2012). Neuropeptide transmission in brain circuits. Neuron *76*, 98–115. https://doi.org/10.1016/j.neuron.2012.09.014.
57. Mykytyn, K., and Askwith, C. (2017). G-Protein-Coupled Receptor Signaling in Cilia. Cold Spring Harb. Perspect. Biol. *9*, a028183. https://doi.org/10.1101/cshperspect.a028183.
58. Rusakov, D.A. (2001). The role of perisynaptic glial sheaths in glutamate spillover and extracellular Ca(2+) depletion. Biophys. J. *81*, 1947–1959. https://doi.org/10.1016/S0006-3495(01)75846-8.
59. Rusakov, D.A., and Kullmann, D.M. (1998). Extrasynaptic Glutamate Diffusion in the Hippocampus: Ultrastructural Constraints, Uptake, and Receptor Activation. J. Neurosci. *18*, 3158–3170. https://doi.org/10.1523/JNEUROSCI.18-09-03158.1998.
60. Macrina, T., Lee, K., Lu, R., Turner, N.L., Wu, J., Popovych, S., Silversmith, W., Kemnitz, N., Bae, J.A., Castro, M.A., et al. (2021). Petascale neural circuit reconstruction: automated methods preprint at bioRxiv. https://doi.org/10.1101/2021.08.04.455162.
61. Kirschen, G.W., Liu, H., Lang, T., Liang, X., Ge, S., and Xiong, Q. (2017). The radial organization of neuronal primary cilia is acutely disrupted by seizure and ischemic brain injury. Front. Biol. (Beijing) *12*, 124–138. https://doi.org/10.1007/s11515-017-1447-1.
62. Cerro, M.P.D., Snider, R.S., and Oster, M.L. (1969). The purkinje cell cilium. Anat. Rec. *165*, 127–130. https://doi.org/10.1002/ar.1091650202.
63. Ono, K., Gotoh, H., Nomura, T., Morita, T., Baba, O., Matsumoto, M., Saitoh, S., and Ohno, N. (2022). Ultrastructural characteristics of oligodendrocyte precursor cells in the early postnatal mouse optic nerve observed by serial block-face scanning electron microscopy. Plos ONE *17*, e0278118. https://doi.org/10.1371/journal.pone.0278118.
64. Silva, M., Morsci, N., Nguyen, K.C.Q., Rizvi, A., Rongo, C., Hall, D.H., and Barr, M.M. (2017). Cell-Specific α-Tubulin Isotype Regulates Ciliary Microtubule Ultrastructure, Intraflagellar Transport, and Extracellular Vesicle Biology. Curr. Biol. *27*, 968–980. https://doi.org/10.1016/j.cub.2017.02.039.
65. Mechaussier, S., Dodd, D.O., Yeyati, P.L., McPhie, F., Attard, T., Shoemark, A., Gupta, D.K., Zariwala, M.A., Legendre, M., Bracht, D., et al. (2022). TUBB4B variants specifically impact ciliary function, causing

a ciliopathic spectrum. Preprint at medRxiv. https://doi.org/10.1101/2022.10.19.22280748.

66. Stepanek, L., and Pigino, G. (2016). Microtubule doublets are double-track railways for intraflagellar transport trains. Science *352*, 721–724. https://doi.org/10.1126/science.aaf4594.
67. Snow, J.J., Ou, G., Gunnarson, A.L., Walker, M.R.S., Zhou, H.M., Brust-Mascher, I., and Scholey, J.M. (2004). Two anterograde intraflagellar transport motors cooperate to build sensory cilia on *C. elegans* neurons. Nat. Cell Biol. *6*, 1109–1113. https://doi.org/10.1038/ncb1186.
68. Tu, H.-Q., Li, S., Xu, Y.-L., Zhang, Y.-C., Li, P.-Y., Liang, L.-Y., Song, G.-P., Jian, X.-X., Wu, M., Song, Z.-Q., et al. (2023). Rhythmic cilia changes support SCN neuron coherence in circadian clock. Science *380*, 972–979. https://doi.org/10.1126/science.abm1962.
69. Ott, C., Elia, N., Jeong, S.Y., Insinna, C., SenGupta, P., and Lippincott-Schwartz, J. (2012). Primary cilia utilize glycoprotein-dependent adhesion mechanisms to stabilize long-lasting cilia-cilia contacts. Cilia *1*, 3. https://doi.org/10.1186/2046-2530-1-3.
70. Loukil, A., Ebright, E., Uezu, A., Gao, Y., Soderling, S.H., and Goetz, S.C. (2023). Identification of new ciliary signaling pathways in the brain and insights into neurological disorders. Preprint at bioRxiv. https://doi.org/10.1101/2023.12.20.572700.
71. Barbour, B., and Häusser, M. (1997). Intersynaptic diffusion of neurotransmitter. Trends Neurosci. *20*, 377–384. https://doi.org/10.1016/s0166-2236(96)20050-5.
72. Henneberger, C., Bard, L., Panatier, A., Reynolds, J.P., Kopach, O., Medvedev, N.I., Minge, D., Herde, M.K., Anders, S., Kraev, I., et al. (2020). LTP Induction Boosts Glutamate Spillover by Driving Withdrawal of Perisynaptic Astroglia. Neuron *108*, 919–936.e11. https://doi.org/10.1016/j.neuron.2020.08.030.
73. Loomba, S., Straehle, J., Gangadharan, V., Heike, N., Khalifa, A., Motta, A., Ju, N., Sievers, M., Gempt, J., Meyer, H.S., and Helmstaedter, M. (2022). Connectomic comparison of mouse and human cortex. Science *377*, eabo0924. https://doi.org/10.1126/science.abo0924.
74. Araque, A., Parpura, V., Sanzgiri, R.P., Haydon, P.G., Araque, A., Parpura, V., Sanzgiri, R.P., and Haydon, P.G. (1999). Tripartite synapses: glia, the unacknowledged partner. Trends Neurosci. *22*, 208–215. https://doi.org/10.1016/s0166-2236(98)01349-6.
75. Perea, G., and Araque, A. (2007). Astrocytes Potentiate Transmitter Release at Single Hippocampal Synapses. Science *317*, 1083–1086. https://doi.org/10.1126/science.1144640.
76. Tereshko, L., Gao, Y., Cary, B.A., Turrigiano, G.G., and SenGupta, P. (2021). Ciliary neuropeptidergic signaling dynamically regulates excitatory synapses in postnatal neocortical pyramidal neurons. eLife *10*, e65427. https://doi.org/10.7554/eLife.65427.
77. Wang, Y., Bernard, A., Comblain, F., Yue, X., Paillart, C., Zhang, S., Reiter, J.F., and Vaisse, C. (2021). Melanocortin 4 receptor signals at the neuronal primary cilium to control food intake and body weight. J. Clin. Invest. *131*, e142064. https://doi.org/10.1172/JCI142064.
78. Cardona, A., Saalfeld, S., Schindelin, J., Arganda-Carreras, I., Preibisch, S., Longair, M., Tomancak, P., Hartenstein, V., and Douglas, R.J. (2012). TrakEM2 Software for Neural Circuit Reconstruction. PLoS ONE *7*, e38011. https://doi.org/10.1371/journal.pone.0038011.
79. Dorkenwald, S., Schneider-Mizell, C.M., Brittain, D., Halageri, A., Jordan, C., Kemnitz, N., Castro, M.A., Silversmith, W., Maitin-Shephard, J., Troidl, J., et al. (2023). CAVE: Connectome Annotation Versioning Engine. Preprint at bioRxiv. https://doi.org/10.1101/2023.07.26.550598.
80. Schindelin, J., Arganda-Carreras, I., Frise, E., Kaynig, V., Longair, M., Pietzsch, T., Preibisch, S., Rueden, C., Saalfeld, S., Schmid, B., et al. (2012). Fiji: an open-source platform for biological-image analysis. Nat. Methods *9*, 676–682. https://doi.org/10.1038/nmeth.2019.
81. neuroglancer 10.5281/zenodo.5573294.
82. Peters, A., Palay, S., and Webster, H.deF. (1991). The Fine Structure of the Nervous System: Neurons and Their Supporting Cells Third Edition (Oxford University Press).
83. Saalfeld, S., Cardona, A., Hartenstein, V., and Tomančák, P. (2009). CATMAID: collaborative annotation toolkit for massive amounts of image data. Bioinformatics *25*, 1984–1986. https://doi.org/10.1093/bioinformatics/btp266.
84. Schlegel, P., Gokaslan, A., and Kazimiers, T. (2022). navis-org/skeletor. Zenodo. https://doi.org/10.5281/zenodo.7308201.

STAR★METHODS

KEY RESOURCES TABLE

REAGENT or RESOURCE	SOURCE	IDENTIFIER
Deposited data		
P36 mouse visual cortex image data	https://www.microns-explorer.org/phase1[26,27]	BOSS: https://doi.org/10.60533/BOSS-2021-GTXY
P54 mouse visual cortex	IARPA MICrONS	BOSS: https://doi.org/10.60533/BOSS-2019-QF8A
P>270 mouse visual cortex	Bock et al.[25]	BOSS: https://doi.org/10.60533/BOSS-2011-K12H
Annotation and processing data	This paper	Zenodo: https://zenodo.org/doi/10.5281/zenodo.10953135
Software and algorithms		
Amira 3D 2021.1	ThermoFisher Scientific	https://www.thermofisher.com/us/en/home/electron-microscopy/products/software-em-3d-vis/amira-software.html
Blender 3.1.2	Blender.org	https://www.blender.org/
CATMAID	Schneider-Mizell et al.[32] Saalfield et al.[78]	https://github.com/catmaid/CATMAID
CAVE	Dorkenwald et al.[79]	https://github.com/CAVEconnectome/CAVEclient
Excel	Microsoft	https://products.office.com/en-us/excel
GraphPad Prism 10 for MacOS	GraphPad Software Inc.	https://graphpad.com
ImageJ2 version 2.14.0/1.54f	Schindelin et al.[80]	https://imagej.net/software/fiji/
Neuroglancer	Martin-Shepard et al.[81]	https://github.com/google/neuroglancer
pycilium	This paper	Zenodo: https://zenodo.org/doi/10.5281/zenodo.10951285

RESOURCE AVAILABILITY

Lead contact

Further information and requests for resources should be directed to the lead contact, Carolyn Ott (ottc@janelia.hhmi.org).

Materials availability

This study did not generate new unique reagents.

Data and code availability

- This paper analyzes existing, publicly available data. Access links for TEM datasets are listed in the key resources table (BOSS: https://doi.org/10.60533/BOSS-2021-GTXY, BOSS: https://doi.org/10.60533/BOSS-2019-QF8A, BOSS: https://doi.org/10.60533/BOSS-2011-K12H). Annotations made to analyze these data are also listed in the key resources table (Zenodo: https://zenodo.org/doi/10.5281/zenodo.10953135) and publicly available as of the date of publication.
- All original code and analysis data products have been deposited at Zenodo: https://zenodo.org/doi/10.5281/zenodo.10951285 and is publicly available as of the date of publication. DOIs are listed in the key resources table.
- Any additional information required to reanalyze the data reported in this paper is available from the lead contact upon request.

EXPERIMENTAL MODEL AND STUDY PARTICIPANT DETAILS

Overview of TEM datasets

The TEM volumes used in this study were collected as a part of collaborative projects designed to determine neuron connectivity. The P36 and P>270 mice have been described.[25–27] The P36 mouse was a triple heterozygote for CamKIIa (Jax:05359), B6;CBA-Tg(Camk2a-tTA)1Mmay/J (Jax: 003010), and GCaMP6f Reporter: Ai93 (JAX024103). The P54 mouse was a cross of B6;CBA-Tg(Camk2a-tTA)1Mmay/J (Jax: 003010) and B6;DBA-Tg(tetO-GCaMP6s)2Niell/J (Jax: 024742). The age of this mouse at perfusion was P54. The P>270 animal was a male Thy1-YFP-H51 mouse. All animal procedures were approved by the Institutional Animal Care and Use Committee at the Allen Institute for Brain Science or Baylor College of Medicine. As detailed with the publication of the original dataset[25] in vivo fluorescent calcium imaging preceded isolation of a volume of the visual cortex from mice. The tissues were then stained, sectioned, and imaged with 4 nm resolution in XY. Section thickness, and thus z resolution is 40 nm. The tissue volumes were

computationally reconstructed by stitching and aligning these images to create a large volume. Neurons were then traced as skeletons directly in the volume,[25] or densely segmented and proofread to generate 3D reconstructions.[28] The heavy metal staining and resolution that makes electron microscopy suitable for neuronal and synaptic reconstruction is sufficient to resolve many intracellular features including nuclear pores, mitochondria cristae, polysomes and microtubules, as well as synaptic vesicles and pre- and post-synaptic densities. Distinguishing features of each dataset including each animal's sex and the area of visual cortex imaged are listed in Table S1.

METHOD DETAILS

Cell classifications

Cell features provided the information necessary for cell classification as described in Peters et al.[82] Excitatory pyramidal neurons were distinguished from the inhibitory neurons based on characteristics including nuclear morphology, axon and dendrite positioning and morphology and the post-synaptic density adjacent to axon termini. In EM, Astrocytes were identified by the dark ring of chromatin around the periphery of the nucleus, the presence of glycogen granules and the many processes that appear to seep rather than project into the surrounding spaces. In segmented data astrocytes were also identified by the characteristic overall cell morphology. Microglia and oligodendrocytes both have small dark nuclei and dark staining cytoplasm but differ in the diameter and content of the processes: oligodendrocyte processes are thin and packed with microtubules while microglia processes narrow more gradually. OPC cells have lighter cytoplasmic staining than oligodendrocytes and microglia. For more details about the identification and characteristics of OPC cells see Buchanan et al.[29]. Astrocytes in P>270 were classified based on the presence or absence of abundant dense intermediate filaments as protoplasmic or fibrous respectively. Many fibrous astrocytes were in cortical layer 1. Cell identities in P36 were manually assigned and accessed via the Connectome Annotation Versioning Engine (CAVE) system.[79] Within the P54 dataset every cell was assigned a cell classification and layer initially based on a clustering analysis of nucleus features.[30] We reconstructed cells based on this initialization then manually confirmed classifications using the morphology of segmented processes. For analysis, layer boundaries in the P54 dataset were defined using a set of manual point annotations based on the size and density of pyramidal cells for each layer to generate average planes dividing L1, L2/3, L4, L5, and L6. Although the P54 volume encompasses layers 1-6, layer 1 was excluded from the 3D segmentation, and thus from our analysis.

Annotation of cilia and centrosomes

For the P36 and P54 volumes, the data was accessed through Neuroglancer[81] and point annotations were used to mark the cilia base and tip, position of each centriole, cilium exit from pocket cilia and vesicles. Skeleton lines were generated by calculating the central path of the segmented structure. Initial annotation and segmentation of P>270 was done using Trak EM2.[78] Annotations were migrated to CATMAID[32,83] and all annotating continued in CATMAID. To facilitate work across multiple datasets, we contracted kazmos GmbH to extend CATMAID to access and annotate data in Neuroglancer precomputed format. This allows all datasets released in this format, including many new and upcoming large EM volumes, to be accessible and annotated from local CATMAID instances without the need to copy data locally. We used CATMAID to trace ciliary skeletons from base to tip in P>270 and to proofread the skeletons created with a central pathline in the P36 and P54 datasets. To locate cilia, we used either the 3D cellular models to identify cilia and then navigated to the corresponding EM images or we searched the somata in the EM volume for centrosomes and then looked to see whether cilia were present. Incomplete cilia were included for measurements of cilia frequency but excluded from other analysis. P36 is the only volume in which every cell in the volume was assessed. In P54 and P>270, cilia in a subset of the abundant excitatory neurons and glia were annotated and all or almost all inhibitory neurons were annotated.

There were astrocytes and neurons in which we were unable to locate a cilium, but these cases were very rare (see Table S2). Cells that left the volume or that had large imaging gaps were excluded from analysis if a ciliated centriole was not found. In the two non-ciliated astrocytes in P36 we found both centrioles in the cytoplasm and are confident that these are nonciliated cells. We are less confident about the absence of cilia in the inhibitory neurons that are not included in the ciliated fraction because we found no centrioles in these cells. It is possible that ciliated centrioles are present and were either overlooked (despite multiple efforts) or obfuscated by imaging gaps or artifacts. In all microglia we found two centrioles. In P36 and P54 all the oligodendrocytes had two non-ciliated centrioles, however, no centrioles were found in any of the oligodendrocytes in P>270. We are not aware of any reports of centriole loss in oligodendrocytes and wonder if the difference could be due to the age difference in the mice. Rare neurons with multiple primary cilia have been found in the hypothalamus.[5] In V1 we observed only monociliated neurons. We did find an astrocyte with cilia extending from both centrioles and another ciliated astrocyte that had a large vesicle associated with the second centriole that appeared to be a pre-ciliary structure. Endothelial cells, part of the brain circulatory system, were omitted from our analysis, however, we did locate pairs of nonciliated centrioles in 3 endothelial cells in the P>270 dataset.

Annotation postprocessing

Analysis of multiple datasets required methods for integrating results across different annotation and data sharing platforms including reading skeletons, meshes, and metadata from a variety of data sources. A python package "pycilium" (github.com/AllenInstitute/pycilium) developed for this project is publicly available on github that allows retrieval of annotations generated using CATMAID, trakEM2, and pre-defined neuroglancer state schemas and supports saving versioned copies of data relevant for subsequent analysis.

Manual segmentation in Amira

Cilia, ciliary vesicles, and the cytoplasm were manually segmented using Amira 3D version 2021.1 (Thermo Fisher Scientific). Cropped image stacks were imported. Next, the cilia structures and cytoplasm created by manually tracing structures in Amira in individual layers. The resulting segmentation was converted into a triangular mesh surface using the 'Generate Surface' module in Amira with constrained smoothing and a smoothing extent of 9.

Re-imaging TEM sections at higher resolution

TEM has the advantage of improved microtubule contrast and the ability to revisit a sample and image again at higher magnification, which is not possible with destructive volume EM methods, such as serial block face scanning EM (SEM) and FIB-SEM (focused ion beam-SEM). Furthermore, TEM enables higher resolution imaging than SEM methods. To obtain higher quality images of cilia identified in the P>270 dataset,[25] we reimaged the same samples with a TEM at higher magnification (JEOL 1200EX). The samples consisting of 1,215 serial sections on Pioloform-coated TEM slot grids were stored in a nitrogen dry box for more than 10 years since the initial imaging. Yet, the new images were comparable to the originals, suggesting that there was minimal sample deterioration during this storage period. Using the published image volume and the original imaging notes as a guide, we identified which grids contained the cilia of interest and located them within each grid. The cilia were imaged at much higher magnifications (30,000x to 65,000x) than previously. Since cilia can extend several microns in length, some cilia required re-imaging from up to 100 sections. For each cilium, the high-resolution serial images were then aligned together using an elastic alignment software pipeline (AlignTK).

Visualization of 3D objects using Blender 3.1.2

3D meshworks of cells, cilia, or processes were imported as wavefront OBJ files. Where necessary, cilia meshworks were isolated and colored separately. For glial cells, the portions of the cell obstructing the view of the cilium were cut away.

Skeleton generation and processing

Skeletons for P36 and P54 were generated using a semi-automated iterative process based on point annotations of the tip and base as well as the mesh derived from the neuronal segmentation. These skeletons were generated by taking a bounding box cutout of a mesh and filtering it by the distance from a line segment between the base and tip of the cilium, then skeletonizing the largest resulting connected component. Subsequent steps filtered the mesh based on a reduced distance from the mesh to the last computed skeleton. Skeletons at each step were generated by thinning with mesh contraction as implemented by the skeletor package[84] followed by mesh based TEASAR and raytracing-based diameter estimation.[31] The resulting skeletons were automatically checked for connectivity to manually defined base, tip, and exit points and reviewed in CATMAID. This process results in a skeleton that approximates the medial axis of the cilium as well as a representative compartment submesh. Skeletons in the P>270 were generated manually by placing nodes at the center of the cilium in each plane. All path lengths used in analysis were derived from these skeletons.

QUANTIFICATION AND STATISTICAL ANALYSIS

Transition zone measurements

Cilia in the P>270 dataset that were sectioned close to parallel to the imaging plane at the cilium base were identified. To measure transition zones, the density between the ciliary membrane and the axoneme was measured in every section where it was visible. Because the transition zone is a periodic structure, the density was not visible in every plane. The variability in measurements from an individual cilium is likely because the cut angle was not precisely parallel. We calculated the mean length for each cilium in Image J / Fiji.[80] For comparison of cilia from different cell classes we calculated a mean and standard deviation weighted by the number of measurements from each cilium.

Quantification of processes adjacent to cilia

Analysis of adjacent processes was possible in the densely segmented datasets (P36 and P54). Using Neuroglancer we navigated to the 2D view anywhere along each 3D structure. We classified each structure based on origin, shape and identifying features. Astrocytic processes were identified based on their characteristic morphology and the presence of glycogen granules. Axons were followed away from cilia until 2 or 3 presynaptic termini were identified. Similarly, the identity of dendrites, which typically have characteristic spines, were verified by locating postsynaptic densities. For 10 astrocytes and 10 excitatory neurons, every process adjacent to the cilium was classified, colored according to type and quantified.

Quantification of dense core vesicles near cilia

In EM DCVs contain an electron dense center that can be used to distinguish them from small clear synaptic vesicles. Cilia in P>270 that were sectioned perpendicular to the imaging plane along the entire cilium were identified. A cylinder with a 1 μm diameter was created around the annotated cilium path length in CATMAID. Each DCV within the cylinder was annotated and the total for each cilium recorded. The sample size is small because few cilia were cross-sectioned along their entire length - most turned in the imaging plane.

Synapse data analysis

The P36 and P54 datasets are linked to volumetric segmentations representing the synaptic clefts of all synapses in each volume.[28,79] To interrogate the spatial relationship between synapses and cilia in neuropil, we queried the 3D skeleton representations of cilia against a PostgreSQL database table with PostGIS support schematized to represent the 3D extents and center points of the segmented synaptic clefts. These queries properly scaled between anisotropic and down sampled segmentation spaces to quantify the distance and distribution of synapses near cilia.

An R-tree representation of synaptic and somatic bounding boxes was used to simulate the effect of placing different model cilia randomly in the volume. Each model cilium, derived from a proofread full cilium from the dataset, was subjected to a rigid transformation defined by a 3D translation picked from a uniform distribution across the bounding box of the synaptic segmentation as well as a random 3D rotation defined by the QR decomposition of a uniformly random 3D matrix. Model cilia were excluded, and the transformation recalculated if they fell within the meshes defining the somatic compartment. The analysis in this paper presented 1000 random transformations for each model cilium.

Analysis of synapses adjacent to cilia and axon process controls as presented in Wu et al.[23] was accomplished with a guided manual process. First, Neuroglancer links were generated with annotations for each automatically identified synapses within 1 micron of each cilium. A subset of these cilia was examined and synapses adjacent to the cilium were marked. To establish the axon control segments, axonal structures with the same cell type as a given ciliated cell were selected in an area on the opposite side of the cell from the cilium. These axon controls were automatically skeletonized and smoothed before being queried against the synapse database for proximal synapses, which were used to generate Neuroglancer links and annotated to mark adjacent synapses. Figures 6G and S6D–S6F calculate the linear regression fit for classes of synapses in a region around an object given its path length using ordinary least squares including a constant, implemented using the statsmodels python package.

Orientation calculations

Ensuring a consistent coordinate space for comparing EM datasets was a non-trivial problem. To address the fact that the V1 datasets used in this study were not natively rendered in a consistent orientation, each dataset was assigned a 3D rigid transformation defined to align the mean orientation of manually defined axon initial segments in layer 2/3 to a consistent rectilinear axis across datasets. This axis, directionally representing the depth from pia to white matter, was used as the zenith when defining spherical coordinate systems and as the axis along which depth was calculated. Polar "rose" plots in Figures 7D and 7E display the angular mean (solid line) as well as the angular standard deviation (dotted lines).

Directional mean and directional standard deviations were found using the following formulations:

Means of trigonometric functions were calculated by averaging the sin and cosine of angles:

$$\overline{S} = 1 \Big/ n \sum_{i=1}^{n} \sin a_i$$

$$\overline{C} = 1 \Big/ n \sum_{i=1}^{n} \cos a_i$$

Angular mean was described using the two-input arctangent of the sin and cosine means

$$\overline{a} = \operatorname{atan} 2(\overline{S}, \overline{C})$$

Angular standard deviation was found with the following formulation:

$$\sigma = \sqrt{\ln\left(1 \Big/ \left(\overline{C}^2 + \overline{S}^2\right)\right)}$$

Morphological calculations

Prior to morphological calculations skeletons were smoothed using a gaussian kernel to mitigate the effects of jitter that arises from inconsistencies in reconstruction and dataset alignment. Tortuosity was calculated as a gross metric ratio of skeleton path length to vector sum length, resulting in possible values [1, inf). Curvature was defined as an instantaneous value describing the inverse of the radius of a circle tangent to the skeleton's path. This calculation was based on a standard formulation defined by the following equation, where gamma is the arc-length parameterization for the curve, implemented in python using the gradient of the smoothed skeleton.

$$\kappa(s) = \| T'(s) \| = \| \gamma''(s) \|$$